NASA/TM–20250001459

Structural Analysis of a 50-m-Tall Thermoplastic Composite Truss Tower Structure for the Lunar South Pole

Andrew C. Bergan, Arunkumar Satyanarayana, and Will J. Grier
Langley Research Center, Hampton, Virginia

Babak Farrokh
Goddard Space Flight Center, Greenbelt, Maryland

Kenneth N. Segal
Goddard Space Flight Center, Greenbelt, Maryland
HelioSpace Corporation, Greenbelt, Maryland

John Chiu
Goddard Space Flight Center, Greenbelt, Maryland
Actalent Corporation, Greenbelt, Maryland

Sandi Miller
Glenn Research Center, Cleveland, Ohio

February 2025

NASA STI Program Report Series

Since its founding, NASA has been dedicated to the advancement of aeronautics and space science. The NASA scientific and technical information (STI) program plays a key part in helping NASA maintain this important role.

The NASA STI program operates under the auspices of the Agency Chief Information Officer. It collects, organizes, provides for archiving, and disseminates NASA's STI. The NASA STI program provides access to the NTRS Registered and its public interface, the NASA Technical Reports Server, thus providing one of the largest collections of aeronautical and space science STI in the world. Results are published in both non-NASA channels and by NASA in the NASA STI Report Series, which includes the following report types:

- TECHNICAL PUBLICATION. Reports of completed research or a major significant phase of research that present the results of NASA Programs and include extensive data or theoretical analysis. Includes compilations of significant scientific and technical data and information deemed to be of continuing reference value. NASA counterpart of peer-reviewed formal professional papers but has less stringent limitations on manuscript length and extent of graphic presentations.

- TECHNICAL MEMORANDUM. Scientific and technical findings that are preliminary or of specialized interest, e.g., quick release reports, working papers, and bibliographies that contain minimal annotation. Does not contain extensive analysis.

- CONTRACTOR REPORT. Scientific and technical findings by NASA-sponsored contractors and grantees.

- CONFERENCE PUBLICATION. Collected papers from scientific and technical conferences, symposia, seminars, or other meetings sponsored or co-sponsored by NASA.

- SPECIAL PUBLICATION. Scientific, technical, or historical information from NASA programs, projects, and missions, often concerned with subjects having substantial public interest.

- TECHNICAL TRANSLATION. English-language translations of foreign scientific and technical material pertinent to NASA's mission.

Specialized services also include organizing and publishing research results, distributing specialized research announcements and feeds, providing information desk and personal search support, and enabling data exchange services.

For more information about the NASA STI program, see the following:

- Access the NASA STI program home page at http://www.sti.nasa.gov

- Help desk contact information:

https://www.sti.nasa.gov/sti-contact-form/

- and select the "General" help request type.

NASA/TM–20250001459

Structural Analysis of a 50-m-Tall Thermoplastic Composite Truss Tower Structure for the Lunar South Pole

Andrew C. Bergan, Arunkumar Satyanarayana, and Will J. Grier
Langley Research Center, Hampton, Virginia

Babak Farrokh
Goddard Space Flight Center, Greenbelt, Maryland

Kenneth N. Segal
Goddard Space Flight Center, Greenbelt, Maryland
HelioSpace Corporation, Greenbelt, Maryland

John Chiu
Goddard Space Flight Center, Greenbelt, Maryland
Actalent Corporation, Greenbelt, Maryland

Sandi Miller
Glenn Research Center, Cleveland, Ohio

National Aeronautics and
Space Administration

Langley Research Center
Hampton, Virginia 23681-2199

February 2025

Available from:

NASA STI Program / Mail Stop 050
NASA Langley Research Center
Hampton, VA 23681-2199

Acknowledgments

The authors gratefully acknowledge the discussions with the NASA Tall Lunar Tower project team especially Matthew Mahlin, William Doggett, and Kyongchan Song. The authors also owe thanks to Ruth Amundsen, Rachel Wiggins, and Amanda Stark for their contributions to the thermal modelling and analysis. Finally, the authors thank Juan Fernandez for discussions on the CTM boom sizing.

Abstract

At the lunar south pole, the sun remains near the horizon and solar arrays can be elevated by truss towers to be exposed to near continuous sunlight. Recent studies suggest that tower heights on the order of 50 m are needed for near continuous sun exposure to meet the power requirements to support a sustained lunar presence. While eventually towers may be constructed using materials sourced in-situ, initially structural elements will likely be brought from the Earth, deployed, and assembled. Thermoplastic composites offer the benefit of high specific stiffness and strength properties along with welding for assembly joints, and therefore represent a promising material system for this application. This report summarizes truss tower structural design, sizing, and analysis undertaken in the Thermoplastics Development for Exploration Applications (TDEA) project for such towers. A set of design requirements are established, and the development of a point design referred to as the Thermoplastic Space Point Design (TSPD) is described. The TSPD is developed and sized through finite element analysis (FEA) and assessed based on available test data. The loading condition that drives sizing is base excitation resulting from moonquakes. This report also describes a set of expressions based on beam theory for preliminary sizing and trade studies of truss tower structures. Results from the TSPD FEA verify the analytical sizing routine and shows the importance of joints in the structural behavior. Trade studies are conducted to evaluate representative materials and truss member cross section profiles. The results show that the TSPD is a viable design and that future efforts with high-modulus thermoplastic composite materials or deployable tube truss members can reduce mass.

List of Symbols

A_L	Longeron cross sectional area
b	Tower width
C_S	Base shear coefficient
E	Young's modulus
f_n	Natural frequency in Hz
F_{axial}	Maximum longitudinal load in truss member
F_L	Maximum compressive force in the longerons
FS	Factor of safety
g_M	Lunar gravitational acceleration
G_{Ic}	Mode I fracture toughness
G_{IIc}	Mode II fracture toughness
H	Tower height
I_L	Longeron cross section second moment of area
I_{truss}	Truss cross section second moment of area
I_x	The second moment of area of the longeron about the axis that minimizes I_{truss}
J	Joint mass penalty factor
k_s	Numerical penalty factor
L	'L' shaped cross section leg length
L_o	Overlap length
L_t	Tab length
L_w	Weld length
M_{eff}	Effective mass of the tower (M_{truss} lumped at top of tower)
M_{truss}	Mass of the truss (tower)
M_{PL}	Payload mass
M_{RSS}	Truss element maximum moment, vector magnitude normal to member axis
r	Frequency ratio
Q	Quality factor (damping)
$R_{d,v}$	Transfer function
R_{TE}	Residual for tower Euler buckling
R_{LE}	Residual for longeron Euler buckling
R_{LS}	Residual for longeron strength
S_{a}	Joint strength allowable
S_A	Spectral acceleration
$S_{A,v}$	Vertical acceleration due to moonquake excitation
t	Member (flange) thickness
T_r	Return period
$\ddot{u}_g$	Ground acceleration
$\ddot{u}_{g,v}$	Ground acceleration in the vertical direction
V	Shear force at tower base
X_c	Compressive strength of the longeron material
β	Damping ratio
β_{ad}	Area reduction factor for the diagonal bracing members
β_{ah}	Area reduction factor for the horizontal bracing members
δ_{tip}	Tower tip, maximum deflection
λ	Eigenvalue
ρ	Density
ω_n	Natural frequency (bending mode)
$\omega_{n,e}$	Extensional natural frequency

List of Acronyms

CFRP	Carbon fiber reinforced polymer
CTM	Collapsible tubular mast
DLL	Design limit load
DSNE	Design Specification for Natural Environments
FEA	Finite element analysis
FEM	Finite element model
FI	Failure index
JSP	Joint splice plate
LM PAEK	Low melt Polyaryletherketone
LSS	Lap shear strength (apparent)
MS	Margin of safety
PSHA	Probabilistic seismic hazard assessment
QI	Quasi-isotropic
RUC	Repeating unit cell
SDEG	Cohesive interface damage variable
SLS	Single lap shear
SMQ	Shallow moonquake
TDEA	Thermoplastics Development for Exploration Applications
TLT	Tall Lunar Tower
TSPD	Thermoplastic Space Point Design
UHS	Uniform hazard spectrum

1 Introduction

Tower structures placed at the lunar south pole that elevate vertically oriented solar arrays can help meet the power requirements needed to support NASA's Moon to Mars Objectives [1]. At the lunar poles, the sun stays near the horizon and so local terrain produces extensive shadowing at ground level. Elevated, vertically oriented solar arrays can obtain near-continuous sun exposure. However, developing a cost-effective capability for lightweight tall towers located near the lunar south pole is a significant structural engineering challenge. While smaller towers might rely on deployed masts [2–4], tower heights greater than ~25 m will likely be trusses [2]. NASA's Tall Lunar Tower (TLT) project [2, 3] developed an approach for robotic structural assembly of a truss tower using riveted metallic connections at the ends of thermoset carbon fiber reinforced polymer (CFRP) square tubes. As part of NASA's Thermoplastics Development for Exploration Applications (TDEA) project, the authors and coworkers developed a variant of the TLT design concept, focusing on structural integrity of an all-thermoplastic CFRP design that can be assembled robotically by welding the members together at the truss nodes. This report focuses on the tower structural analysis and sizing conducted by the TDEA team.

This report is organized as follows. First, the tower structure design requirements established in TDEA are described. Then, the structural design and sizing activities are described in section 3, leading to the Thermoplastic Space Point Design (TSPD). This section includes a description of the preliminary sizing, design-analysis iterations, preliminary thermo-structural analysis, joint analysis, and an assessment using available test data near the end of the TDEA project. While the TSPD design and analysis iterations were underway, the approach used for preliminary analysis was further developed [4]. This updated structural sizing approach is described in section 4, and the results from trade studies conducted using this tool are provided in section 5. The trade study results show the significance of selected design assumptions in the TSPD and identify opportunities for future work that can lead to reduced structural mass.

2 Design Requirements

The TSPD is designed around a set of requirements assumed in the TDEA project, mostly inherited from the TLT project [2, 3]. The requirements are listed in Table 1. The requirements are organized into two groups: (A) those prioritized and addressed by the TDEA project, and (B) those recognized as likely required for a complete flight system but not addressed in the TSPD, mostly due to resource limitations of the TDEA project. Requirements A.1 and A.2 come directly from NASA STD 5001B [5] and the 2.0 factor of safety on discontinuities is interpreted to apply to welded assembly joints. At the time these requirements were developed, the lander or foundation structure on which the tower would be deployed was not defined and so a fixed rigid base was assumed (A.3). The loading is assumed to be lunar gravity (A.5) and base excitation from moonquakes (A.6). Moonquakes are thought to occur at the lunar south pole, yet many unknowns exist regarding lunar seismic activity [6]. A harmonic base excitation with amplitude of 0.15 g_M is assumed herein based on the predicted peak ground acceleration at 60 km from an epicenter in [7]. While the predictions in [7] focus on the transient response, moonquake events recorded by the Apollo missions (e.g., [8, 9]) had durations of several hours, and so a steady-state excitation is assumed here. In section 4, an alternative assumption for moonquake loading, the uniform hazard spectrum (UHS) reported in [10], is considered.

Table 1. Design requirements used for the TSPD.

#	Requirement name	Parameter	Reference
A.1	Positive margin of safety (mechanical load)	> 0	5001
A.2	Composite material FS	1.5 uniform material 2.0 discontinuities	5001
A.3	Payload mass (M_{PL})	$M_{PL} = 1000$ kg	Assumed
A.4	Base interface	Fixed base, 4 corners	[3]
A.5	Lunar gravity (g_M) load	$g_M = 1.62$ m/s^2	
A.6	Dynamic loads	Harmonic base excitation, $\ddot{u}_g / g_M = 0.15$	Assumed
B.1	Joint alignment feature	Repeatable joint positioning ≤ 1 mm	TLT
B.2	Robotic grip interface at joint	Baseline 15.2 mm diameter ball at end of fitting.	TLT
B.3	Base interface during assembly	Fixed at 4 robotic grip interfaces	TLT
B.4	Positive margin of safety (thermomechanical load)	Predicted temperature extremes: Hot: 55 °C; Cold –240 °C	Temperatures from TLT
B.5	Assembly temperature	–240 °C	Temperature from TLT
B.6	Assembly in vacuum	Test to 10^{-5} Torr	
B.7	Weld contamination	Lunar dust simulant with TBD particle concentration (mass/unit area)	
B.8	Radiation durability	Positive margin after TBD dose	DSNE 3.4.7
B.9	Micrometeoroid durability	Survive TBD particle impact event	
B.10	Thermo-structural durability	Survive TBD spectrum fatigue loadings	
B.11	Max joint weld time	Not defined	
B.12	Max welding power	Not defined	
B.13	Structure packaged volume	Not defined	
B.14	Structure mass (M_{truss})	Not defined	
B.15	Max tip deflection (δ_{tip})	Not defined	
B.16	Electrical grounding	Not defined	

The remaining requirements (B.#) in Table 1 are identified but not addressed in the TSPD. Requirements B.1–B.3 regard robotic assembly and were developed previously by TLT team. The TSPD design is developed so as not to directly conflict with these requirements, but design and analysis were not specifically conducted to address B.1–B.3. Structural margins are not addressed for thermo-structural loads (B.4), which can be important especially at the joints (see [11] for a qualitative assessment). Requirements B.5–B.7 address the assembly environment in which welded joint operations would be performed. Requirement B.7 addresses the observation that lunar dust contamination was prevalent during the Apollo missions [12] and so some level of lunar dust on surfaces prior to welding is probably unavoidable. However, no rationale or data was readily available to quantify the level of contamination for B.7. In the TDEA project, welds

with varying levels of lunar dust simulant were conducted to provide some initial data on the weld strength sensitivity to lunar dust simulant contamination, but those tests and test results are outside the scope of this report. Requirements B.8–B.10 consider structural durability. Requirement B.9, micrometeoroid durability, may introduce novel structural engineering challenges since traditional shielding may not be practical for a large, assembled tower structure. The remaining requirements B.11–B.16 are identified as potentially important but not developed further. It is noted that the maximum tip deflection (B.15) is likely relevant, especially for communications and navigation payloads that may be co-manifested and can drive the structural design and sizing.

3 TSPD Structural Sizing

The TSPD structural design and sizing is developed through design and analysis iterations to the prioritized requirements (A.1–A.6). This section describes the TSPD structural design and analysis starting with preliminary sizing that led to the tower cross section dimension, then several iterations with finite element analysis (FEA) that led to the structural member designs, and, finally, analysis and sizing of the welded joints. This section concludes with a summary of test data that became available since the TSPD was developed, its implications for the TSPD, and planned future tests.

3.1 Preliminary Sizing

Preliminary sizing of truss towers can be performed using a set of expressions based on beam theory and an iterative solution method to identify promising designs, e.g., [2, 3, 13]. The approach used here extends [2, 3, 13] by including base excitation (moonquake) loads and consideration for longeron strength. In the preliminary sizing, harmonic base excitation was assumed to represent shallow moonquake (SMQ) loads (see [9–12, 17] for discussion of moonquake event characteristics).

3.1.1 Governing Equations

A prismatic truss tower is assumed with height, H, and square cross section with width, b, as shown in Figure 1. The truss comprises four longerons located near the corners such that b is measured to the outside of the member cross section (overall width). The longerons have cross section area, A_L, and second moment of area, I_L, and are constructed with material having a Young's modulus in the axial direction, E. The longerons are stabilized by horizontal and diagonal members.

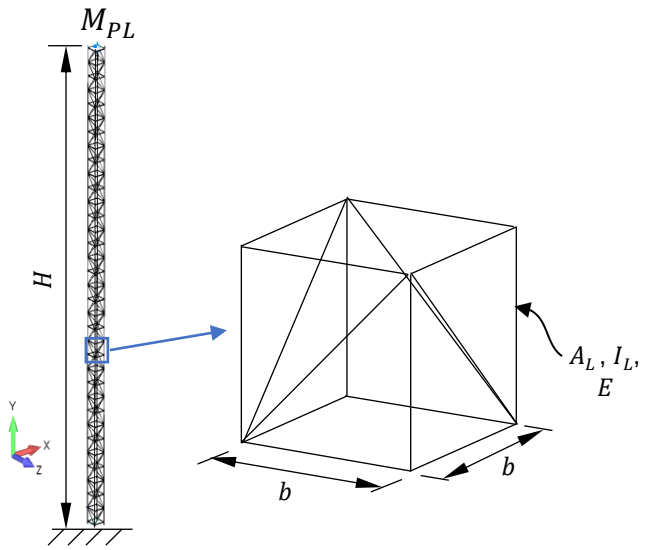

Figure 1. Prismatic truss tower, with the truss connectivity assumed following [2, 3].

The longerons are sized for positive margins on tower buckling, longeron buckling, and longeron strength. A residual for tower Euler buckling is calculated as

$$R_{TE} = \frac{\pi^2 E I_{\text{truss}}}{4H^2 FS} - M_{\text{eff}} g_M - M_{\text{eff}} S_{A,v} \tag{1}$$

where the first term is the buckling limit scaled by the factor of safety, FS, the second term is the static load due to gravity, the third term is additional dynamic load due to base excitation in the vertical direction. The effective mass M_{eff} is the mass of payload, M_{PL}, and the fraction of the mass of the truss M_{truss} lumped at the top of the tower [14]

$$M_{\text{eff}} = M_{PL} + 0.3 M_{\text{truss}} \tag{2}$$

M_{truss} is defined in [2] as

$$M_{\text{truss}} = A_L H \rho J \left(4 + 4\beta_{ah} + 5\sqrt{2}\beta_{ad}\right) \tag{3}$$

where ρ is the density of the material, β_{ah} and β_{ad} are area reduction factors for the horizontal and diagonal bracing members which may have smaller cross sections than the longerons, and J is a nondimensional joint factor that represents the mass penalty of the joints. β_{ah}, β_{ad}, and J are user defined parameters. Herein, it is assumed that $\beta_{ah} = \beta_{ad} = 0.7$ and $J = 1.3$ following [2]. It is perhaps not intuitive that (3) is independent of b, but this occurs since cubic bays are assumed. The second moment of area of the truss I_{truss} is calculated as

$$I_{\text{truss}} = 4I_x + A_L b^2 \tag{4}$$

where I_x is the second moment of the area of the longeron about the axis that minimizes I_{truss}. In [2], it is assumed that I_x is negligible. Vertical acceleration due to moonquake excitation ($S_{A,v}$) is included in the third term of (1) since SMQ events are thought to induce horizontal and vertical ground accelerations with similar magnitudes, e.g., [7]. For harmonic ground motion, $S_{A,v}$ can be calculated assuming the vertical ground acceleration is the ground acceleration, $\ddot{u}_{g,v} = \ddot{u}_g$, and $S_{A,v} = \ddot{u}_{g,v} R_{d,v}$ where $R_{d,v}$ is a standard transfer function (see, e.g., [15])

$$R_{d,v} = \frac{1}{{\omega_{n,e}}^2} \frac{1}{\sqrt{(1-r^2)^2 + (2\beta r)^2}} \tag{5}$$

with the damping ration, β, and the frequency ratio, r, calculated using $\omega_{n,e}$ as

$$r = \omega/\omega_{n,e} = \omega\left(\frac{4A_L E}{M_{\text{eff}}H}\right)^{-1/2} \tag{6}$$

For most practical designs, $r \ll 1$, $\omega_{n,e}\sim 1$, and therefore $R_{d,v} \leq 1$. Herein, $R_{d,v} = 1$ is used as a conservative assumption. The bending mode natural frequency of the tower with payload mass M_{PL} is obtained from [16] as

$$\omega_n = \sqrt{\frac{\frac{\pi^4 E I_{\text{truss}}}{32H^3} - g_M\left(\frac{\pi^2(2M_{PL} + M_{\text{truss}}) - 4M_{\text{truss}}}{16H}\right)}{M_{PL} + (3\pi - 8)M_{\text{truss}}/2\pi}} \tag{7}$$

where the numerator is the bending stiffness of the tower, and the denominator is the tower mass where the factor $(3\pi - 8)/2$ accounts for the effective truss mass at the tip (see [14] or [16]). In (7), vertical acceleration due to moonquakes is ignored.

To calculate residuals for strength and buckling of the longerons, the maximum compressive force in the longerons, F_L, is assumed to occur near the base of the tower. F_L is the sum of the force due to axial compression of the tower (last two terms in (1)) and the force due to the bending moment resulting from the horizontal base excitation

$$F_L = \frac{M_{\text{eff}}}{4}\left(g_M + \ddot{u}_{g,v}\right) + \frac{H}{2b}C_S(\omega_n)(M_{PL} + 0.23M_{\text{truss}})g_M \tag{8}$$

The first term is negligible in most cases. In the second term, $C_S(\omega_n)$ is the nondimensional base shear coefficient, which is a function of the natural frequency, in general. For harmonic base excitation, the tower is assumed to resonate and so C_S is

$$C_S = \frac{\ddot{u}_g/g_M}{2\beta\sqrt{1-\beta^2}} \tag{9}$$

Using (8), residuals for longeron strength and buckling are

$$R_{LS} = \frac{X_c A_L}{FS} - F_L \tag{10}$$

$$R_{LE} = \frac{\pi^2 E I_L}{b^2 FS} - F_L \tag{11}$$

respectively, where X_c is the compressive strength of the longeron material and I_L is assumed to be calculated about the axis that produces a minimum. In the first term in (11), the Euler buckling load for the longeron is calculated assuming the truss comprises bays having height b and free rotation of the truss nodes so the end conditions are pin-pin, which is a conservative assumption since the joint has some stiffness.

3.1.2 Solution Method

With the residuals defined in (1), (10), and (11), the sizing of the truss is defined by longeron cross sectional parameters A_L and I_L, and the tower width b. The problem is to minimize these residuals subject to constraining A_L, I_L, and b to be practical values (i.e., greater than some small positive value) where we assume that near zero margin minimizes the structural mass.[1] The values for

[1] A more conventional approach in the truss optimization literature is to minimize the mass subject to constraints defining the design criteria. Since buckling introduces a nonlinear constraint, the numerical solution is challenging, and some type of linearization is usually required, e.g., [40]. The present approach circumvents this issue.

β_{ah}, β_{ad}, and J are considered fixed. Small positive residuals (positive margin) are much more desirable than small negative residuals, so the total residual is calculated as

$$\mathbb{E} = \sum_{i=TE,LE,LS} \left[R_i\left(k_s + \mathbb{H}(-R_i)(1-k_s)\right)\right]^2 \tag{12}$$

where $\mathbb{H}(x)$ is the Heaviside operator and k_s is a small positive number such that the error scales $1/k_s$ slower when the residual is positive. The solution is obtained by minimizing (12) using the solver feature in Microsoft Excel. The starting point and bounds are selected to aid the solution routine based on engineering judgement and trial-and-error to limit trial solutions to practical values. The results described below are local minima not limited by arbitrary bounds.

3.1.3 'L'-shape Cross Section Properties

Various member cross sections were considered for the TSPD. Near the start of the effort, the 'L' shaped cross section was down selected since it provides a good compromise between structural efficiency and volumetric packaging efficiency as described in [2]. Considering the section schematic shown in Figure 2, the section properties are calculated as follows [3].

$$A_L = 2Lt - t^2 \tag{13}$$

$$I_L = I_{a2} = \frac{t(2L^4 - 4L^3t + 8L^2t^2 - 6Lt^3 + t^4)}{12(2L-t)} \tag{14}$$

$$I_x = \frac{t(5L^2 - 5Lt + t^2)(L^2 - Lt + t^2)}{12(2L-t)} \tag{15}$$

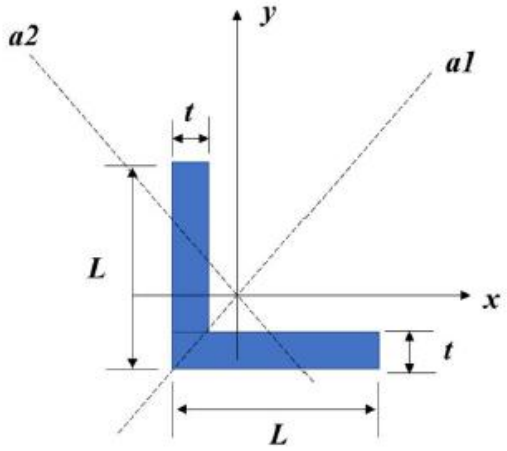

Figure 2. 'L' shape cross section schematic, [3].

With the assumed 'L' shape cross section, the sizing routine is solved for flange thickness, t, and tower width, b.

3.1.4 Results

The analytical sizing scheme described above was applied to evaluate the design space and help guide where to focus follow-on FEA efforts. The sizing routine was applied for four values of $\ddot{u}_g/g_M$ and three values of E for a total of 12 cases. In the analysis, $H = 50$ m, $L/t = 10$, $M_{PL} = 1000$ kg, $FS = 1.5$, and $\beta = 3\%$. The material properties $\rho = 1600$ kg/m^3 and $X_c = 350$ MPa are selected to be representative of CFRP composite laminates. The results are summarized in Figure 3a, where the 16 circular markers correspond to the 16 cases noted above. Annotations show the maximum tip deflection (δ_{tip}) and tower mass (M_{truss}) for selected cases at the corners of the examined design space. These preliminary results were used to select a tower width $b =$

1.5 m. The selection of $b = 1.5$ m was somewhat arbitrary and mostly based on keeping the tip deflections reasonable. This tower width was also selected to be conservative to proceed with FEA holding b constant and avoid time-consuming modeling iterations. The preliminary analyses were repeated for $H = 15$ m to address the case where cable stays support the tower up to a height of 35 m. It is assumed that the unsupported remaining 15 m of tower height behave as if rigidly fixed where the cable stays terminate. FEA was used in a limited study of cable-stayed-designs as described in Appendix A, but ultimately, cable stays were not pursued for the TSPD.

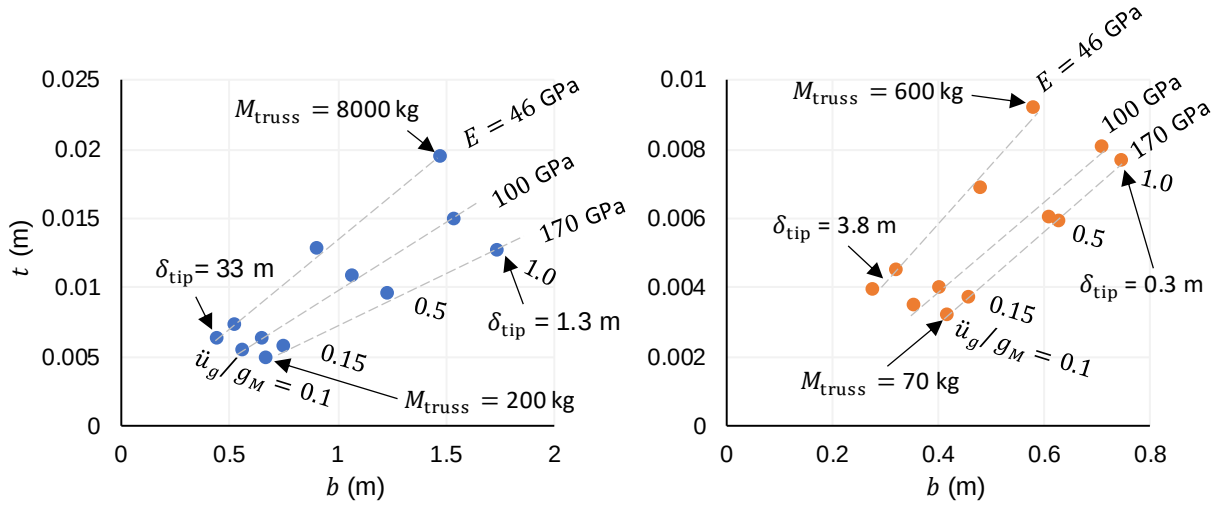

(a) $H = 50$ m (b) $H = 15$ m

Figure 3. Results of preliminary sizing studies.

3.2 Design and Analysis Development

FEA was used to develop the TSPD through design-analysis iterations. Early on, it was evident that the base excitation (moonquake) is the most severe load case, and so efforts focused on achieving positive margins for strength and buckling with the assumed resonance due to a moonquake event. This section describes the detailed analysis approach, iterations, and the final TSPD configuration. Throughout this section, the material is TC1225 (LM PAEK) T700GC 12k with lamina consolidated ply thickness of 0.138 mm. Material properties and strength allowables used in analyses and margin calculations are adopted from [17].

3.2.1 Analysis Approach

Two different finite element modeling approaches were used to assess the performance of the TSPD structure under relevant loading conditions. The two modeling approaches used beam and shell elements, respectively, to represent the tower members. Since accounting for the section behavior in buckling analysis is important, the shell element model was used for most of the work. The load cases include a static body load due to the gravity (A.5) and a sinusoidal base excitation dynamic load case representing an assumed moonquake event (A.6).

The beam-based finite element model (FEM) is at an intermediate level of fidelity that lies between the analytic model (section 3.1) and the shell element FEM that was developed subsequently. The models and their resolution are shown in Figure 4. The beam element model has the advantage of allowing quick evaluations of different section properties, with a discrete representation of the truss geometry. While in the analytical model, the horizontal and diagonal members are assumed to be rigid, the beam element model includes their compliance. However, the beam model is limited in that the welded joints are represented by nodes at the intersections of longeron, horizonal, and diagonal members. Although the beam model can capture the overall behavior of the tower structure (e.g., natural frequencies of the tower shown in Figure 5), it

overpredicts the stiffness of the joints and the overall tower structure (and therefore the natural frequencies). The beam element model also proved useful for verifying the analytical model, which occurred later on in the project, and is described in section 4.4.

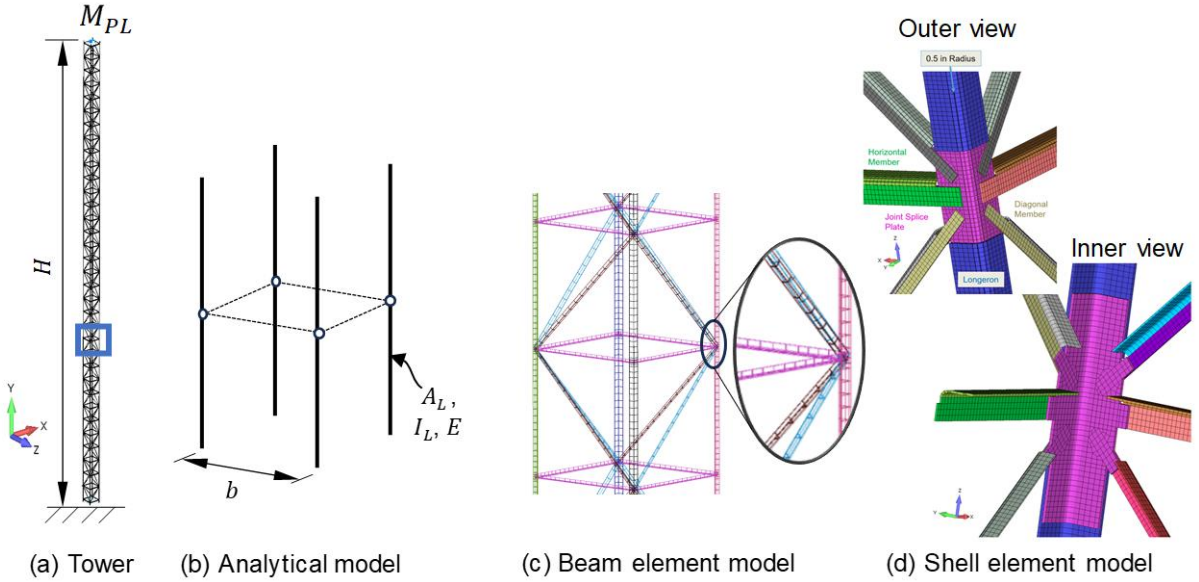

Figure 4. Tower with schematics showing the three levels model fidelity used in this study.

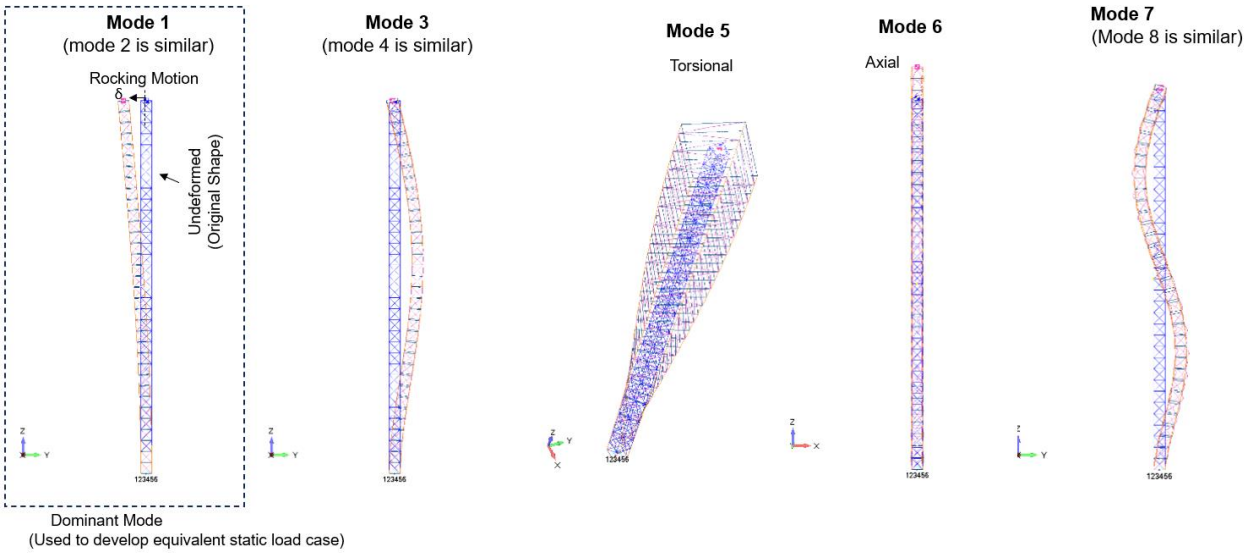

Figure 5. Typical modes of vibration for the TSPD tower beam FEM from 0.1 Hz to 10 Hz.

To mitigate the shortcomings of the beam element model, a shell element model including both the L-section members and joint splice plates was used for most of the analyses, as shown in Figure 4d. The shell model was created in Femap [18] and solved in Simcenter Nastran [19]. The model includes around 562,000 shell elements representing the truss members and joint splice plates, having a typical element edge length of 13 mm. At joint locations, the truss members connect to a joint splice plate with duplicate elements sharing the same nodes and appropriate

section offsets, as shown in Figure 6b.[2] The laminate properties for the truss parts were calculated based on lamina properties (mean values) reported in [17] for the layups determined through design-analysis iteration. The material 0° -direction is along the axis of the 'L'-shaped members (Figure 6a). The corner radius evident in Figure 4d was added during design analysis iterations (not included in the initial version of the model). The tip loads (or the concentrated mass element) and fixed-base boundary conditions are implemented at single nodes at the top and bottom and are connected to the shell mesh with RBE2 rigid elements. Results were evaluated 1 repeating unit cell (RUC) above the fixed base since the actual base boundary condition is not defined or modeled. The joint region was only considered in terms of stiffness in these models. Joint sizing for strength was addressed with a separate model and is described in section 3.4.

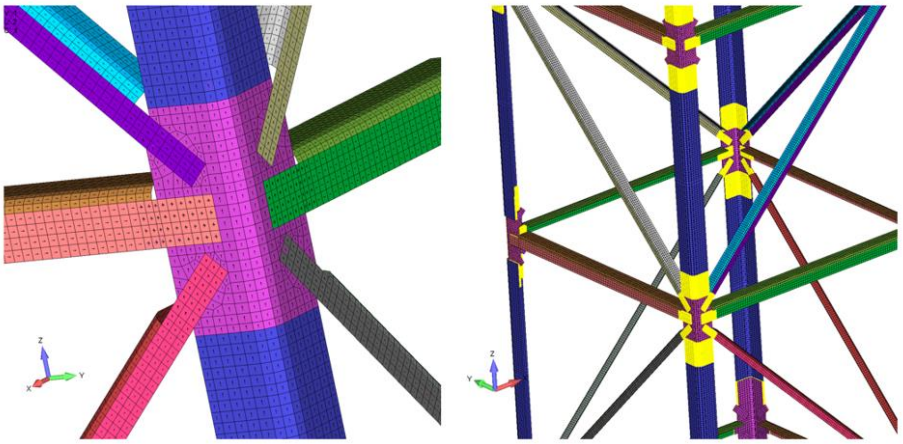

(a) Material directions
(Along the axis of each member)

(b) Duplicated elements with
offset (highlighted) at the welded interface

Figure 6. Details of high fidelity TSPD shell FEM.

Due to the nature of the structure and loads, the base excitation (moonquake) dynamic load case is the dominant load case and the design driver. Dynamic analysis was performed to obtain the response of the tower to a base excitation of $\ddot{u}_g/g_M = 0.15$ from 0.1 Hz to 10 Hz with an assumed Quality (Q) factor of 15 for damping. The first mode (natural frequency) of vibration is a lateral rocking mode (Figure 5) that causes tip deflection. To evaluate strength and buckling margins, the maximum tip deflection δ_{tip} from the dynamic analysis was used as an enforced displacement in subsegment stress and buckling analyses. Stress margin calculations were carried out using factors of safety of 1.5 and 2 for the composite truss members and at joints, respectively, while a factor of safety of 1.5 was implemented to calculate margins against buckling failure (requirements A.1 and A.2). Figure 7 illustrates an overall sizing and structural analysis flow for the TSDP truss structure.

[2] This modeling choice was intended to allow for evaluation of the joints (e.g., using the Virtual Crack Closure Technique). However, no such evaluation was done. As a result, for the purpose of the present study the model is essentially equivalent to an idealization where a single layer of shell elements is used throughout with thicker section definitions for the single lap joint regions.

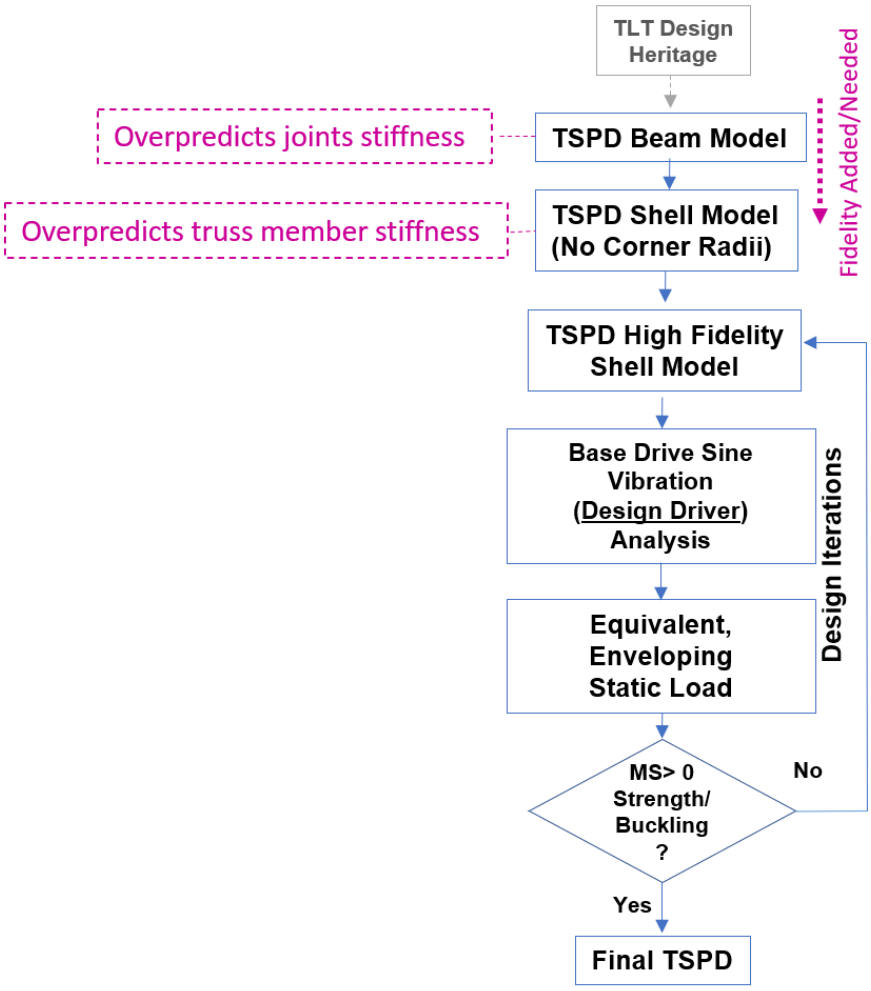

Figure 7. TSPD structural analysis approach flow diagram.

3.2.2 Design Iterations

A baseline design concept was adopted and matured through design and analyses iterations to meet the A.1–A.6 requirements. The truss connectivity is the same as in [13] (no other truss configurations were considered). The design comprises longitudinal members braced with diagonal and horizontal members. The members are joined at the truss nodes with a joint splice plate (JSP) using single lap type connections, as shown in Figure 8. As noted above, $b = 1.5$ m is fixed and so the resulting truss architecture is seventeen RUCs such that $H = 51$ m. With these assumptions, the design parameters defined through design-analysis iteration are the geometry of the 'L' sections (i.e., width and thickness), layups, and the jointing scheme, including the geometry of the JSP. The slender tower is a stiffness-driven structure and so the design is driven by buckling with the moonquake-induced load. The result of the design-analysis iterations is shown in Figure 8. The member cross sections were made wider and thicker, partially to offset the reduction in stiffness due to the corner radius that was necessary for manufacturability. The JSP stiffness was also found to be critical. The baseline design included tabs on the JSP such that overlaps between the JSP and bracing members were offset away from the longitudinal member axis to improve accessibility for the welding operation. This design was found to be too flexible and so alternative options were considered to stiffen the joint region. The final design is shown in Figure 8 where the bracing members extend farther toward the tower corners, which stiffens the joint. An alternative configuration was considered where the orientation of the bracing

members was changed so that they could extend with full cross section toward the corners of the tower, as shown in Figure 9. This configuration did not appreciably improve the design margins and so it was not pursued further.

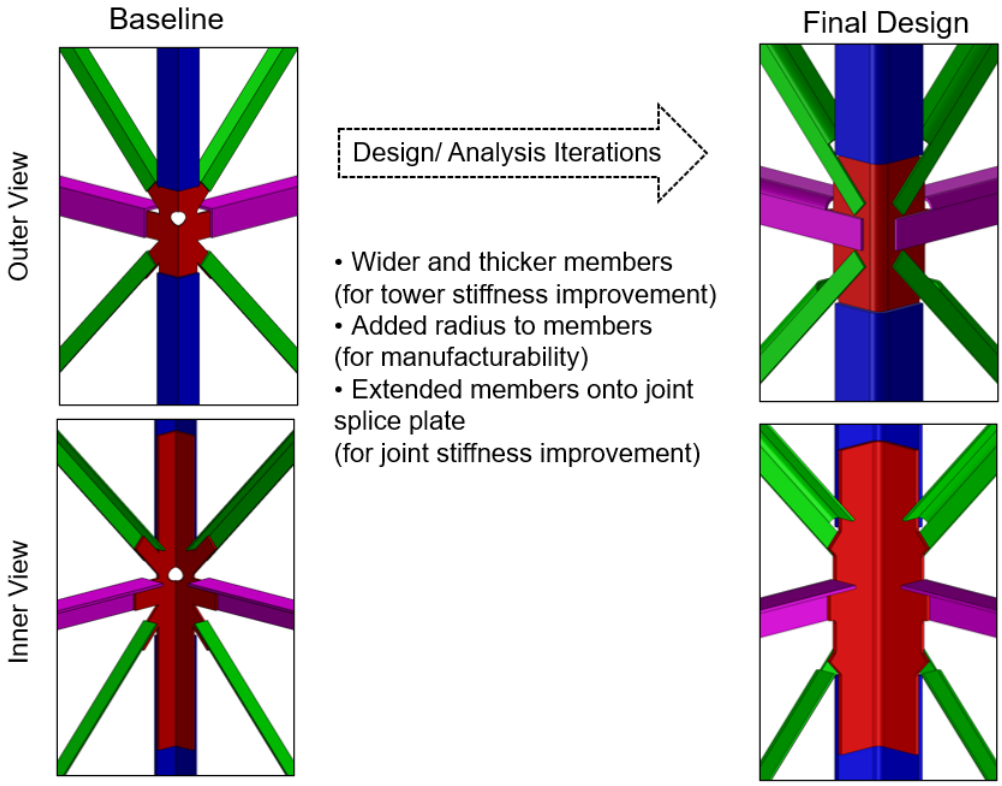

Figure 8. TSPD design iterations to meet A1–A6 requirements.

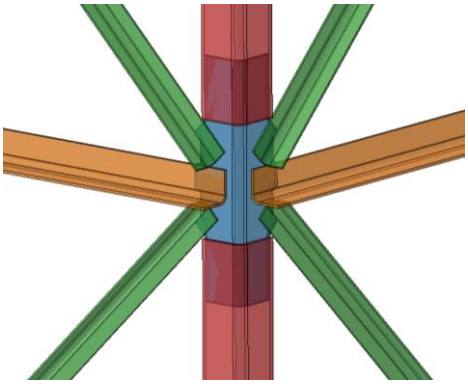

Figure 9. Alternative configuration with rotated, unnotched horizontal and diagonal members.

3.2.3 Final Design and Analysis Results

The final configuration of the TSPD tower is shown in Figure 10 and the component thicknesses and respective layup schedules are summarized in Table 2.

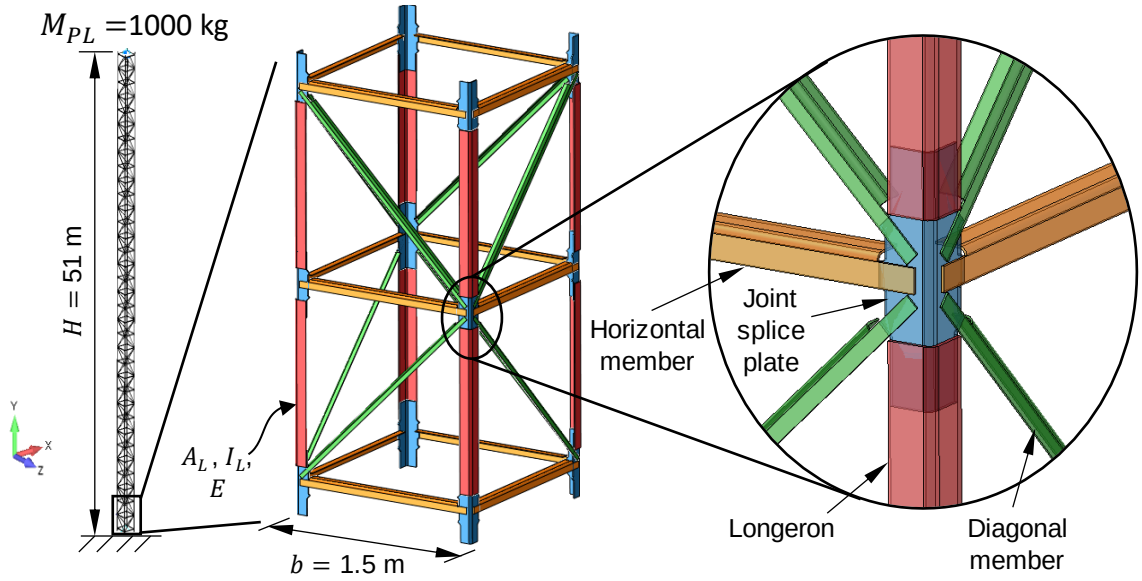

(a) Full tower (b) Repeating unit cell (RUC) (c) Typical joint

Figure 10. TDEA point design. The joint region is shown with transparency so that the overlap (welded) regions are visible.

Table 2. Final TSPD member sized and layup schedule. Dimensions in mm.

Member	Thickness, t	Flange length, L	Layup
Vertical	8	98	$[(45/0_2/-45/0_2)_4/0_6]_s$
Joint splice plate	7	114	$[45/90/-45/0_{10}/(45/90_2/-45/0_9]_s$
Horizontal	5	69	$[(45/0_2/-45/0_4)_2/0_2/\bar{0}]_s$
Diagonal	4	49	$[(45/0_2/-45/0_2)_2/0_3]_s$

The tower design is driven by the base excitation load assumed to represent a moonquake event, which excites the first lateral mode of the tower and results in $\delta_{\text{tip}} \approx 0.8$ m (equivalent to a point load of 4.7 kN). The 4.7 kN is then used as an input load for subsequent linear static and buckling analyses. Figure 11 shows the failure index contour of the TSPD tower under the 4.7 kN design limit load. A maximum failure index (FI) of 0.13, which occurs in the JSP near the tower base, indicates a healthy margin against strength failure (FI = 1 indicates first ply failure based on max strain failure criterion). The buckling requirement is more critical as previously mentioned. The final design has a buckling eigenvalue of 1.6 (exceeds the 1.5 requirement) and the mode is shown in Figure 12. Finally, a summary of truss member axial loads, F_{axial}, and moments, M_{RSS}, at a height of one RUC from the base of the tower is provided in Table 3. The moment magnitudes are the vector magnitude (root of sum of squares) in the plane normal to the member axis.

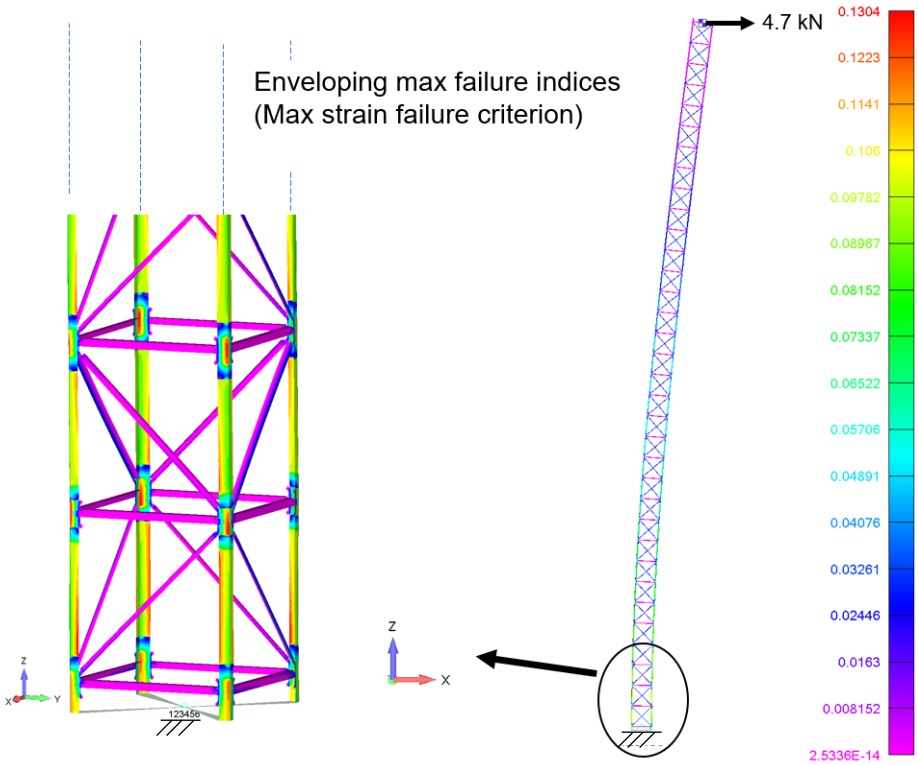

Figure 11. Failure index contour of the TSPD under 4.7 kN design limit load. The deformed tower is plotted on the right-hand side with a deformation scale factor of 5.

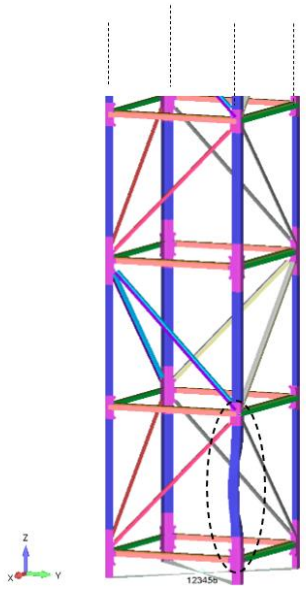

Figure 12. TSPD first buckling mode (λ = 1.6) under design limit load.

Table 3. Design limit load (DLL) summary: maximum internal forces and moments at one RUC above the tower base.

Member	F_{axial} [kN]	M_{RSS} [N-m]
Longitudinal	74.0	113.0
Diagonal	3.3	49.5
Horizontal	0.5	3.8

3.3 Preliminary Thermo-structural Analysis

A preliminary thermo-structural analysis was conducted to ensure that the final design is capable of globally withstanding the temperature gradients and subsequent thermal distortions and stresses. The analysis scope is limited to one down-selected thermal analysis case: a sunlit tower with a shadowed base (additional cases should be examined in future work). This particular case was selected because it is one of the most severe in terms of temperature gradients. The predicted temperature profile generated by Thermal Desktop (for details on the thermal analysis, see [11]) was mapped to the structural model and it is shown in Figure 13.

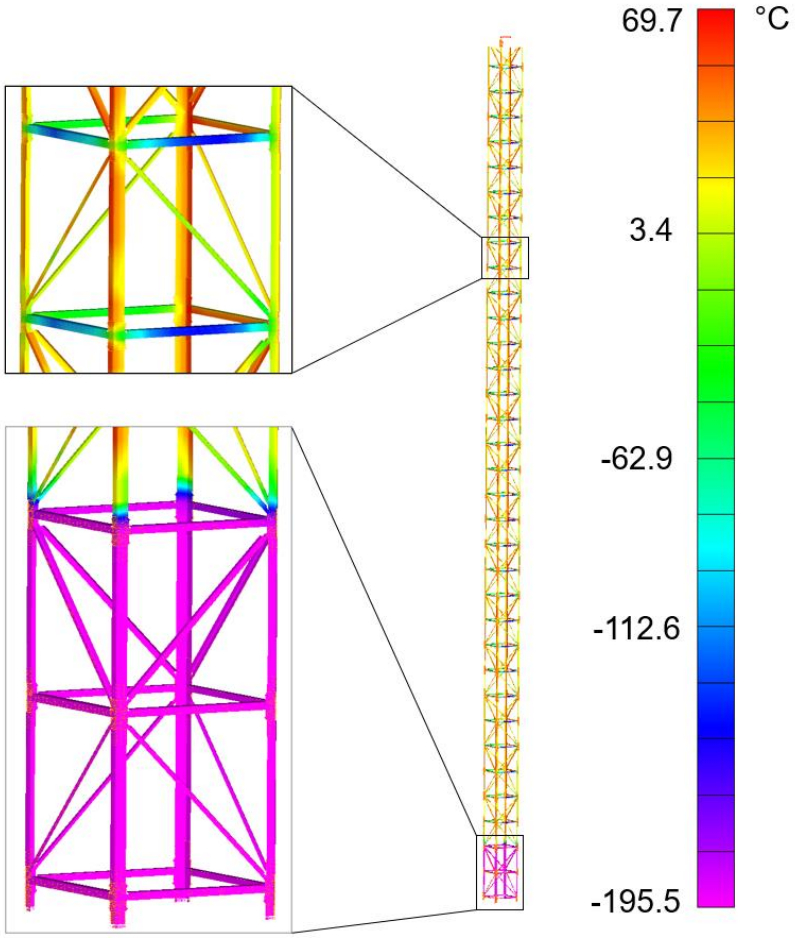

Figure 13. Mapped temperature profile from thermal to the structural model.

The temperature profile shown in Figure 13 is used as an input load case in linear static analysis to obtain the thermally induced stresses and distortions. The analysis uses room temperature properties and a reference temperature of –181 °C as an assumed temperature at the lunar surface at the time of assembly. The global response shows a relatively small distortion (~7.5 mm), Figure 14, and low stress magnitudes, which result in positive margins of safety. The maximum failure index (calculated using the maximum strain failure criterion) is located at the connection between the horizontal member and JSP, Figure 15, likely due to the stiffness mismatch since the two parts have 0°-dominated layups. A higher-fidelity analysis is needed to assess the response of the welded interface at joints to the thermal environment with consideration for thermal residual stresses induced during welding.

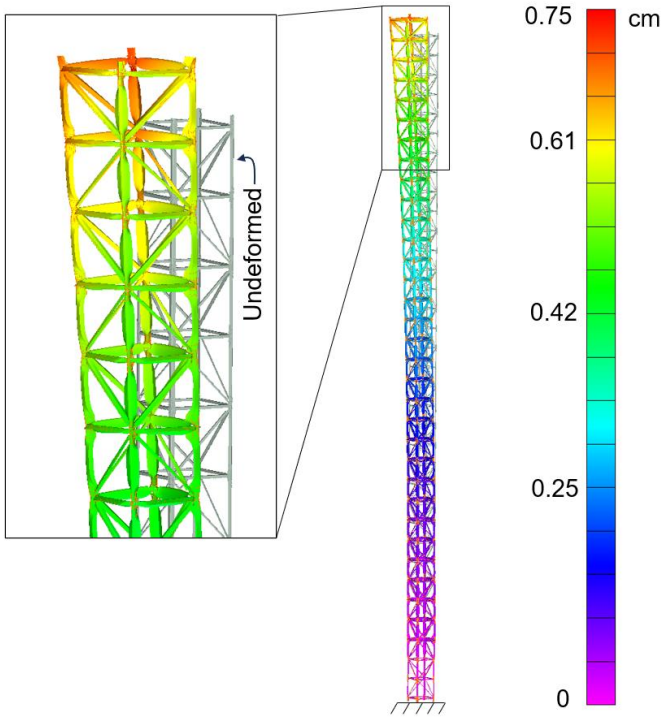

Figure 14. TSPD tower thermal distortion contour.

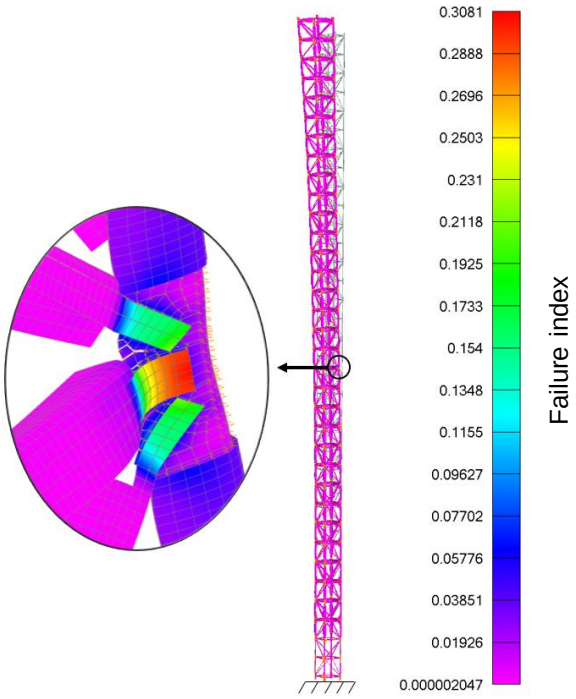

Figure 15. TSPD tower failure index contour from thermal gradient load case.

3.4 Longitudinal Joint Strength Predictions

The joint strength analysis focuses on the connection between the longitudinal member and JSP (denoted as the vertical joint) since the longitudinal members carry most of the load. The objective of the joint strength analysis is to predict the weld area required to achieve positive margin. A simplified FEM of this joint was created, as shown in Figure 16. Joint strength analysis was conducted in parallel with the structural element sizing described previously. Since the overall structural sizing of the tower was evolving when this analysis was conducted, several coarse assumptions were made for simplicity. The geometry and loads associated with the diagonal and horizontal members are ignored, and the JSP is simplified to a prismatic 'L' section. A quasi-isotropic layup is assumed for both the JSP and vertical members. The structural elements are meshed with continuum shell elements (SC8R) using Abaqus [20]. Lamina material properties are used for the elastic material behavior [17]. The weld interface between bracket and vertical member is modeled using zero-thickness cohesive interface elements (COH3D8). The width of the welds is 48 mm, which reflects the assumption that it is not possible to weld to an edge. The unwelded overlapped region is modeled with a contact condition. Five weld lengths $L_w = 38$, 76, 114, 152, and 191 mm are evaluated. Weld interface fracture toughness is assumed to be the interlaminar toughness ($G_{Ic} = 2.1$ kJ/m^2 and $G_{IIc} = 2.6$ kJ/m^2 [21]). The interface strengths are calculated following [22] such that 5 elements are in the process zone for the 0.5 mm element size used in the model. A bilinear traction separation law is assumed. End shortening displacement was applied to the vertical member and the model was analyzed using Abaqus/Explicit.

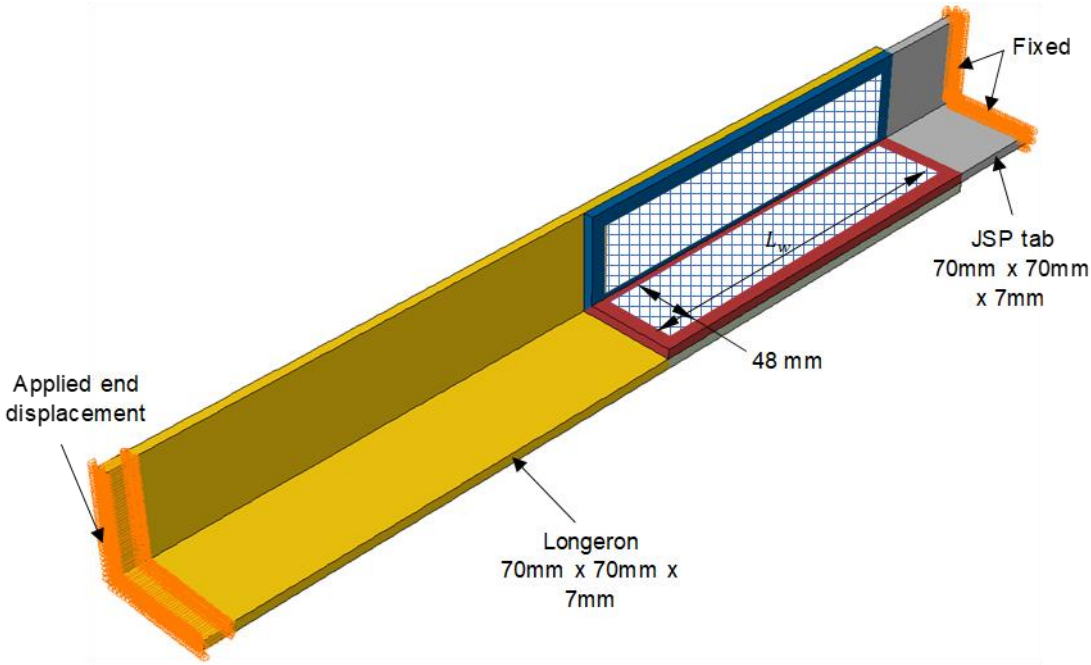

Figure 16. Overview of the model used for joint strength prediction. The cross-hatched region is welded.

The analysis predictions for failure load vs. end shortening for the five weld lengths are presented in Figure 17. With increasing weld length, the stiffness and strength of the FEM increase. The joint strength is predicted to meet 2 DLL at a length of about 90 mm. These results also highlight that the joint strength approaches a plateau for weld lengths greater than 150 mm. Separate analysis showed that the compression load case is the design driver (more severe than tension). These results supported the selection of a 114-mm weld length in the final design.

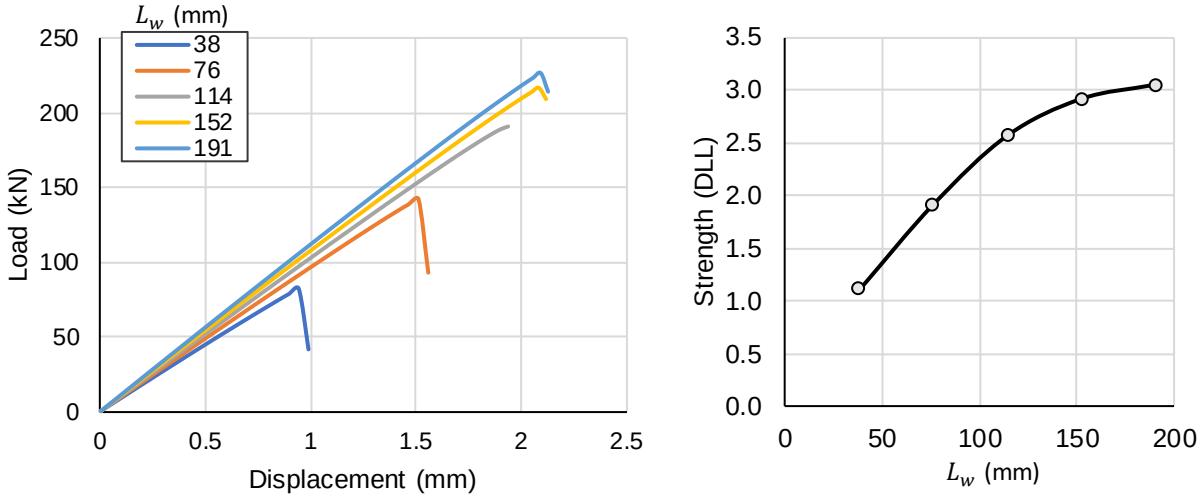

Figure 17. Joint strength predictions.

The cohesive interface damage (SDEG in Abaqus) representing the status of the weld interface at max load, just before failure, is shown in Figure 18 for all the weld lengths. Blue indicates the weld is intact (no damage, SDEG=0) and red indicates the weld is failed (fully damaged, SDEG=1). The model predicts that damage will start near the corner of the 'L' section in all cases.

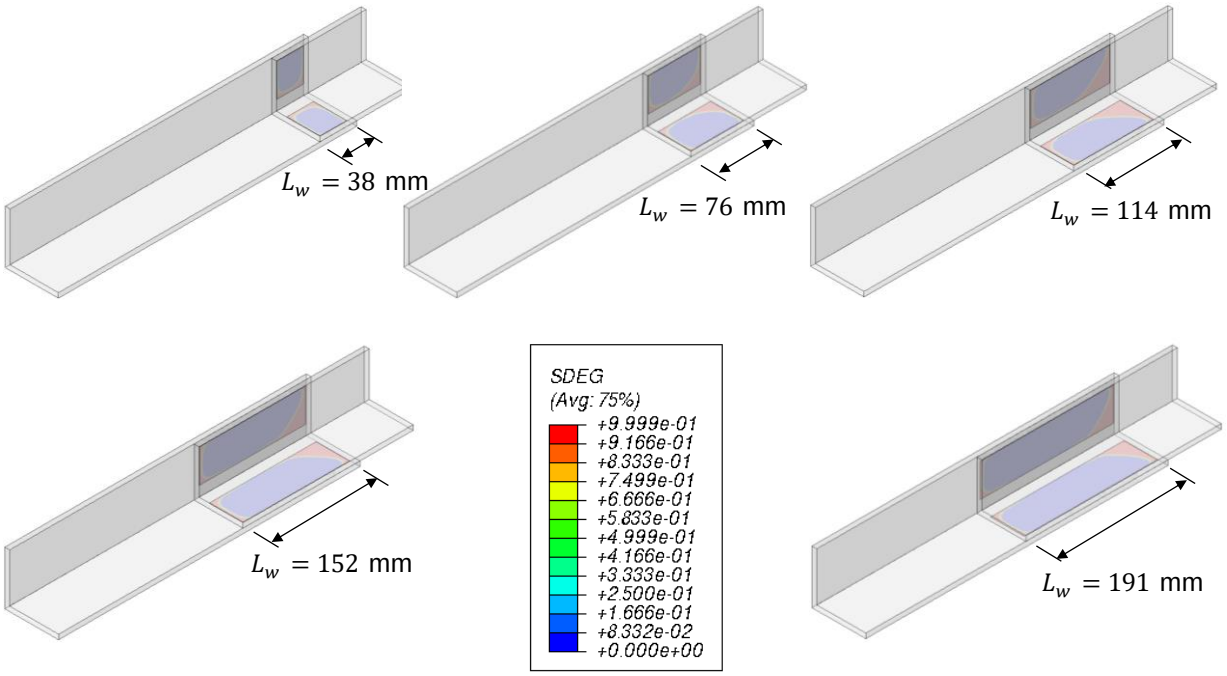

Figure 18. Predicted damage contours just before failure.

3.5 Design Assessment Using Available Test Data

Coupon and sub-element tests were planned and conducted in TDEA to validate the weld strength and structural design of the longitudinal joint in the TSPD (also referred to as the TSPD vertical joint). Ultrasonic welding was selected as the welding approach and a series of tests were planned to develop the ultrasonic welding process for the TSPD application. The TSPD vertical joint is a single lap joint geometry similar to the ASTM D5868 coupon configuration [23] but with an 'L' section, larger overlap length and width, and thicker adherends. Therefore, much of the coupon weld process development effort was conducted using single lap shear (SLS) specimens. However, lap shear strength (LSS) is known to be specific to the joint geometry and layup. LSS cannot be applied directly to assess the TSPD joint margins, i.e., the vertical joint margin of safety can be expressed as

$$\text{MS} = S_{\text{a}}/(FS * F_{\text{axial}}) - 1 \tag{16}$$

where S_{a} is the joint strength allowable, which in general is not equal to the LSS. Instead, we assume that fracture toughness along an idealized weld interface is the appropriate similitude parameter that is independent of joint geometry and layup. Therefore, predictions of LSS and vertical joint strength are correlated using fracture toughness. This section describes the implementation of this approach leading to target LSS required to achieve a vertical joint with positive margins (in (16), MS > 0). It should be noted that this analysis ignores 1) potential workmanship/process difference between the SLS coupon and the full-size vertical joint welds, 2) difference in fracture mode mixity between the SLS and vertical joint, and 3) the effect of layup orientations on failure modes. Extending this analysis to a breakout model of the TSPD vertical joint such that the TSPD loading of the joint is considered as opposed to the simplified loading used for in the vertical joint sub-element test configuration is also potential future work. Alternatively, S_{a} can be obtained from the sub-element tests. However, the analysis here provides relationships to estimate S_{a} using simpler and much less expensive test data.

A series of analyses were conducted to generate curves relating LSS to the TSPD vertical joint strength. The models all use a single layer of cohesive elements at the weld interface to represent the connection between the adherends and predict joint strength, as described in section 3.4. The model used for the LSS prediction is shown in Figure 19. The typical SLS

specimens had dimensions: $L_a = 102$ mm, $L_o = L_w = L_t = 25.4$ mm, and a 25.4 mm width. Initial weld process trials used 16-ply quasi-isotropic (QI) adherends.

An updated version[3] of the vertical joint model described in section 3.4 is used for the vertical joint strength prediction and is shown in Figure 20. This updated model was developed for analysis of the sub-element test configuration of the vertical joint. As a result, it includes the geometry and boundary conditions of the sub-element test, meant to represent the vertical joint in the TSPD.

As a step towards the vertical sub-element geometry, layups, and larger weld area, different SLS configurations were manufactured and tested. One configuration included specimens having 52-ply, 0°-dominated layup referred to as thick adherend SLS. A second configuration was a larger SLS specimen ($L_a = 140$ mm, $L_o = 70$ mm, $L_w = 57$ mm, and $L_t = 25.4$ mm) referred to as weld setback specimens. Models were developed for both of these configurations as well.

All the models described in the preceding three paragraphs were analyzed for a series of fracture toughnesses up to the interlaminar fracture toughness. $2G_{Ic} = G_{IIc}$ is assumed in all SLS analyses except for the result using interlaminar fracture toughness values. A well consolidated weld is expected to have fracture toughness greater than the interlaminar fracture toughness [24] and so the result for interlaminar fracture toughness is relevant as a target for what should be achievable. The predicted correlation in strengths for the different specimen configurations are shown in Figure 21 and Figure 22. The relationships are essentially linear for the ranges considered. The results in Figure 21 indicate that sub-element strength of at least 2 DLL requires 16-ply QI LSS > 17 MPa. The adherend geometry plays a significant role in LSS, as evident in Figure 22, where it is shown that the LSS from the thick adherend welds should be almost twice as high as the thinner adherends if the weld process produces weld interfaces with equivalent properties.

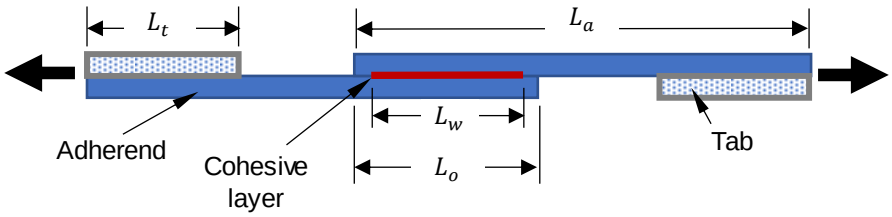

Figure 19. Schematic of model used to predict LSS.

[3] The geometry, layups, and boundary conditions are updated from the model described in section 3.4 and the meshing and analysis approach are the same.

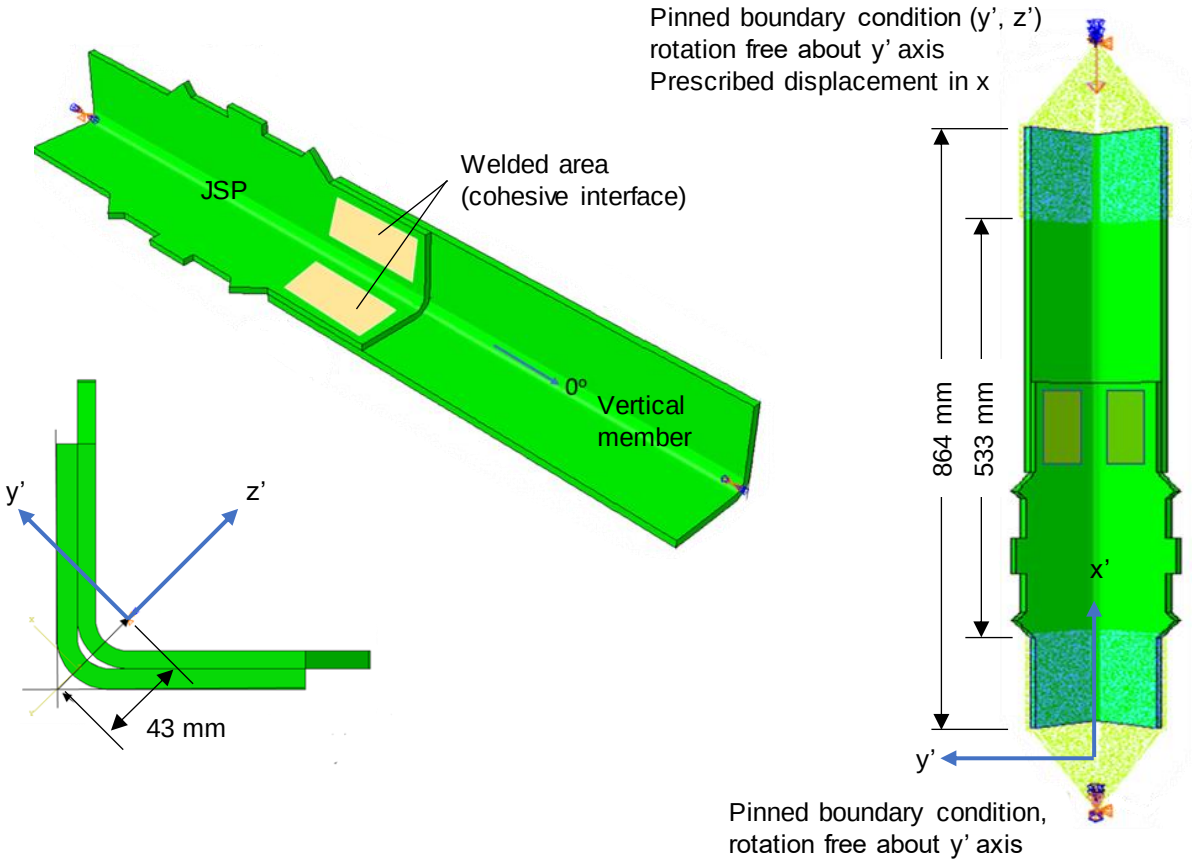

Figure 20. TSPD vertical joint sub-element model.

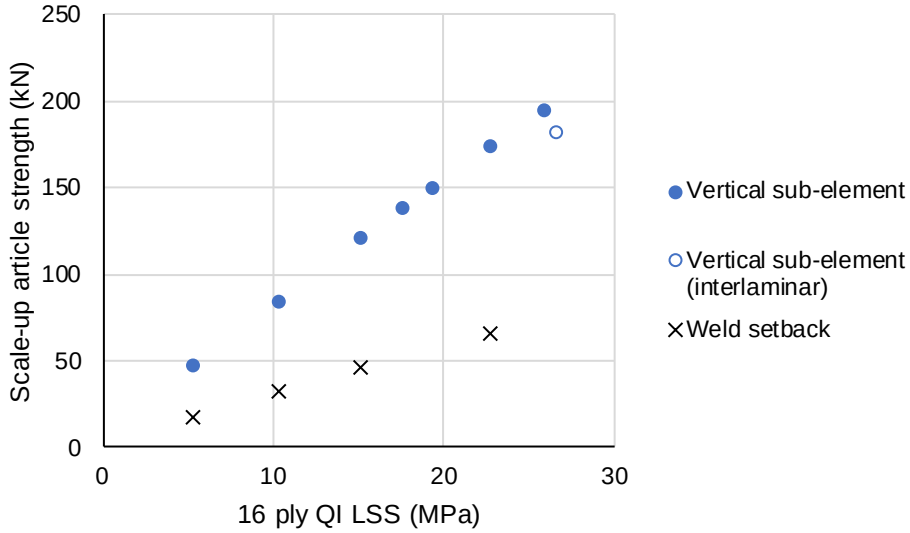

Figure 21. Predicted relationship between 16-ply QI LSS and scaled-up article strengths for weld setback and vertical sub-element configurations.

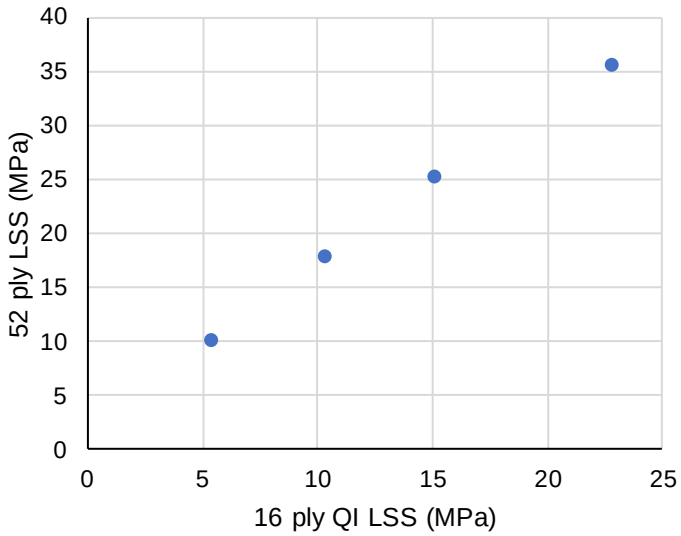

Figure 22. Predicted relationship between LSS for 16-ply QI adherends and 52-ply 0°-dominated adherends.

4 Updated Structural Sizing Approach

The preliminary sizing described in section 3.1 was updated later in the TDEA project and verified using the FEM described in section 3.2.1. The updates include use of a uniform hazard spectrum representation of moonquake loads, inclusion of alternative cross sections, and a more robust optimization routine. This section describes the updates and verification. A brief discussion on the relationship between factors assumed in the preliminary sizing routine and those obtained from the FEA-based design-analysis iterations is included. The following section describes results of parametric studies completed using the update sizing approach.

4.1 Moonquake Excitations and Tower Loads

The seismic events that result in the most severe shaking are called shallow moonquakes (SMQ) [8]. Some characteristics of SMQ differ significantly from earthquakes, including much longer event durations (> 1 hr). Recent simulations of SMQ events [9, 10, 28] provide a basis for ground excitations relevant for designing structures that can sustain such events. Watters et al. [6] provide a characterization of seismicity and preliminary assessment of slope stability for Artemis missions in the lunar south pole region. Ruiz et al. [10] reported a preliminary probabilistic seismic hazard assessment (PSHA) focused on the Apollo 17 landing site, which was later applied to habitat design [25]. The need for additional lunar seismic data has been recognized as a priority and is being addressed with the Farside Seismic Suite, which will provide long term measurement of seismic data [26].

The uniform hazard spectra (UHS) reported in [10] is used herein for tower structure design. The UHS for 2% and 10% probability of exceedance in 50 years (return periods $T_r = 2500$ years and 475 years, respectively) are reproduced in Figure 23 in terms of the nondimensional base shear coefficient,

$$C_S = S_A(\omega_n)/g_M \tag{17}$$

and frequency. $S_A(\omega_n)$ is the spectral acceleration as a function of natural frequency and $g_M = 1.6$ m/s^2 is lunar gravity. C_S is a convenient parameter since the shear force at the tower base is $V = C_S W$ where W is the weight of the tower. Since the tower structure designs considered herein can have natural frequencies, $f_n = \omega_n/(2\pi)$, that are relatively low, we assume the UHS curve can be linearly extrapolated as shown by the dashed line.

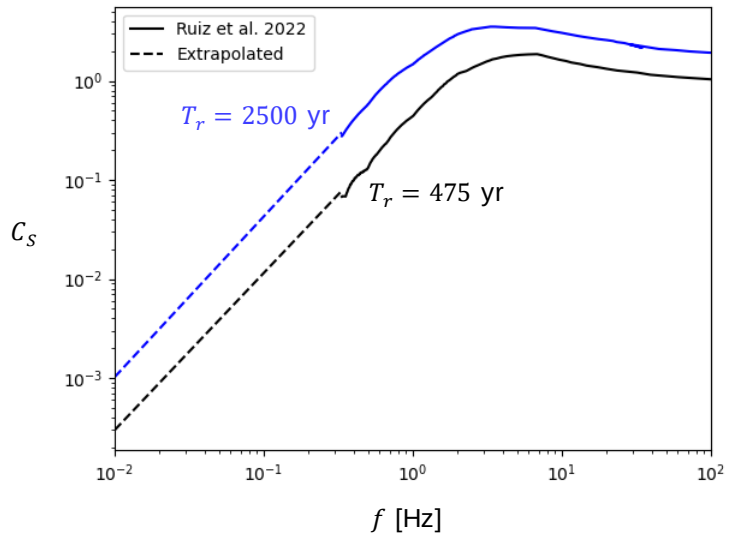

Figure 23. Uniform hazard spectra from [10] replotted in terms of base shear coefficient.

One important observation from the measurements made during the Apollo missions is that SMQ event duration can be greater than 1 hour. In that case, analysis using a shock response spectrum approach may be inadequate. Therefore, we consider a harmonic excitation as a simplistic alternative, as was done in sections 2 and 3. Since f_n is in the range of excited frequencies, resonance is assumed as in section 3.1. Since resonance is assumed, (9) is independent of frequency. In the TDEA project, $\ddot{u}_g/g_M = 0.15$ was assumed along with a typical structural damping $\beta = 3.3\%$. In this case, $C_S = 2.27$ which, when compared to Figure 23, produces much higher loading for $f_n < 0.5$ Hz. Further analysis is needed to develop a more rigorous estimation for tower loads. In this report, the results are calculated using (9) except as noted otherwise (for the purpose of highlighting the significance of the assumed loads). Since the dynamic loads vary with the tower stiffness, mass, and damping, an iterative numerical solution is required.

4.2 Alternative Cross Section Shapes

The 'L' section shape was selected for the TSPD for volumetric packaging efficiency and manufacturability. Early iterations of the TSPD assumed an 'L' with no fillet. However, most manufacturing approaches, including the automated fiber placement selected by TDEA, require a fillet at the corner where the two flanges meet. FEA results showed sensitivity to the inclusion of a fillet, which is expected since it changes the section's second moment of area. Expressions for I_L and I_{truss} were implemented for arbitrary 'L' section fillet radius by treating the fillet as a collection of piecewise linear segments following the approach in [27]. The effect of the fillet radius is summarized in Figure 24, where it can be observed that I_L is more sensitive than I_{truss} and so longeron buckling is the margin most sensitive to the fillet radius, which is consistent with the findings from the FEA iterations.

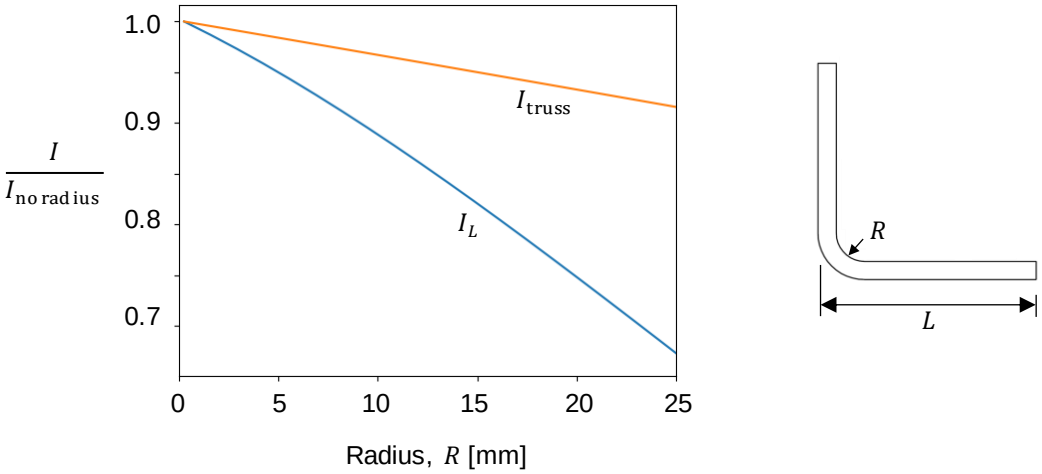

Figure 24. Normalized second moment of area for 'L' section longerons and trusses with variable fillet radius, R.

While closed-section tubes made with thermoset composites are readily manufactured and available, aerospace-grade thermoplastic composite tube manufacturing is at a lower TRL and much less readily available. Nonetheless, the relatively thick cross sections determined for the 'L' section TSPD motivate exploration of more structurally efficient approaches. Therefore, three additional closed cross-section shapes were considered. The first two are relatively conventional round and square tube shapes. Following the approach for the 'L' section, the ratio of width (or diameter) to wall thickness is held constant so that the structural member section size is defined by one parameter. This ratio should be selected to avoid local buckling modes. In general, the closed sections are much more structurally efficient. The third cross is the lenticular collapsible tubular mast (CTM) [28], as shown in Figure 25. Again, simplifying assumptions are made to define the section size with a single parameter: $r_1 = 150t$, $r_1 = 2\,r_2$, $w = r_2/3$, $\alpha_1 = \alpha_2 = 90°$, $t_w = 2t$. The CTM is a deployable structure designed such that the section can be flattened and rolled. Therefore, it offers both high structural and volumetric packaging efficiency.

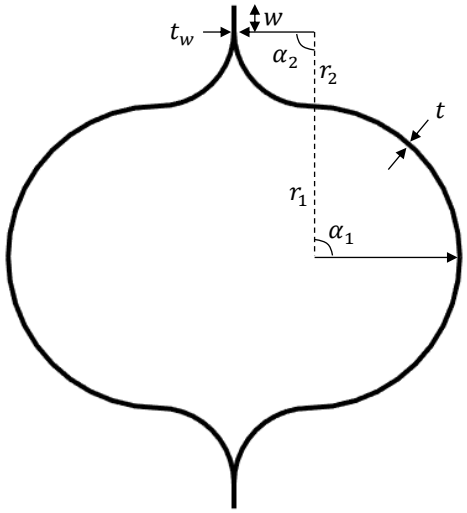

Figure 25. Collapsible tubular mast cross section.

4.3 Solution Method

In the updated structural analysis, the dual annealing method [29] available in SciPy [30] is used to obtained a solution by minimizing (12). The dual annealing method is a stochastic global

optimization algorithm that explores the solution space by selecting the next trial point close to the current one if the objective function is within a tolerance that decreases through the solution history. Bounds are provided to aid the solution routine based on engineering judgement and trial-and-error to limit trial solutions to practical values. The results described below are minima located away from the bounds.

4.4 Verification

Initial verification of the proposed method is obtained by comparison of the longeron strength and buckling loads with the results of a FEM constructed with beam elements. The model represents the truss members for $H = 51$ m, $b = 1.5$ m, and with nonstructural mass for the payload $M_{PL} = 1000$ kg. The longerons are assumed to have symmetric L-shaped cross sections with flange thickness $t = 5$ mm and a flange length, L, of 50 mm ($L/t = 10$ assumed so that flange buckling can be ignored). Nonstructural mass is included at the joints corresponding to $J = 1.3$. The material is assumed to be a 0°-dominated laminate of TC1225 T700/LM-PAEK thermoplastic composite having longitudinal modulus $E = 92$ GPa, density $\rho = 1600$ kg/m^3, and compressive strength $X_c = 350$ MPa [17]. The FEM was fixed at the base and several analyses were run. The bending and axial frequencies were obtained from a modal analysis using the FEM and found to be 0.22 Hz and 8.6 Hz, respectively, which were reproduced by the analytical expressions within 2%. An FEM eigenvalue buckling analysis was used to analyze tower buckling and yielded a buckling load within 1% using analytical Euler buckling from the first term on the right-hand-side (RHS) of (1). Then, a dynamic analysis was conducted for harmonic base excitation sweep from 0.1 Hz to 10 Hz with $\ddot{u}_g/g_M = 0.15$ and $\beta = 3.3\%$, which produced a maximum tip deflection of 1.9 m at resonance. Using this deflection as representative of the static equivalent load, the maximum longeron load was obtained from a quasi-static analysis and is 5% of the value calculated by (8). The longeron buckling load from the FEM is about twice the value obtained from the first term on the RHS of (11), which is not surprising since the joint is rigid in the FEM and its rotation is resisted by the diagonal and horizontal bracing members whereas the longeron is treated as having pinned ends in (11). Considering that the joint stiffness is likely overestimated by the beam-element FEM, the conservatism in (11) is assumed acceptable.

The total residual in (12) is calculated using the model parameters defined above ($H = 51.3$ m, $L/t = 10$, $M_{PL} = 1000$ kg, $J = 1.3$, $E = 92$ GPa, $X_c = 350$ MPa, $\rho = 1600$ kg/m^3, $\beta = 3.3\%$, $FS = 1.5$) for a range of t and b values. This is visualized as a contour plot in Figure 26 for harmonic ground motion and the UHS with $T_r = 475$ years. In both cases there is a clear local minimum, which is found by the optimization routine (cyan-colored circle). The curves corresponding to zero residuals in equations (1), (10), and (11), are shown with the brown, pink, and olive-colored markers. These curves indicate zero margin with positive margin being above and to the right of the curves. For harmonic ground motion, longeron buckling and strength size the structure, whereas for the UHS, tower Euler buckling and longeron buckling size the structure. For the UHS load case, the longeron strength margin R_{LS} is relatively independent of b since the longeron load F_L is also relatively insensitive to b. R_{LS} happens to be near zero for this set of parameter values but can drive sizing when other values are specified. The optimal design for the UHS loading has a larger b and smaller t and so it is lighter. Using $T_r = 2500$ years, b is about the same but t increases by about 30%. Zero-margin designs show rather gradual increases in t when changing b slightly from the optimal value. When b is reduced significantly to around 0.3 m, the required t increases rapidly.

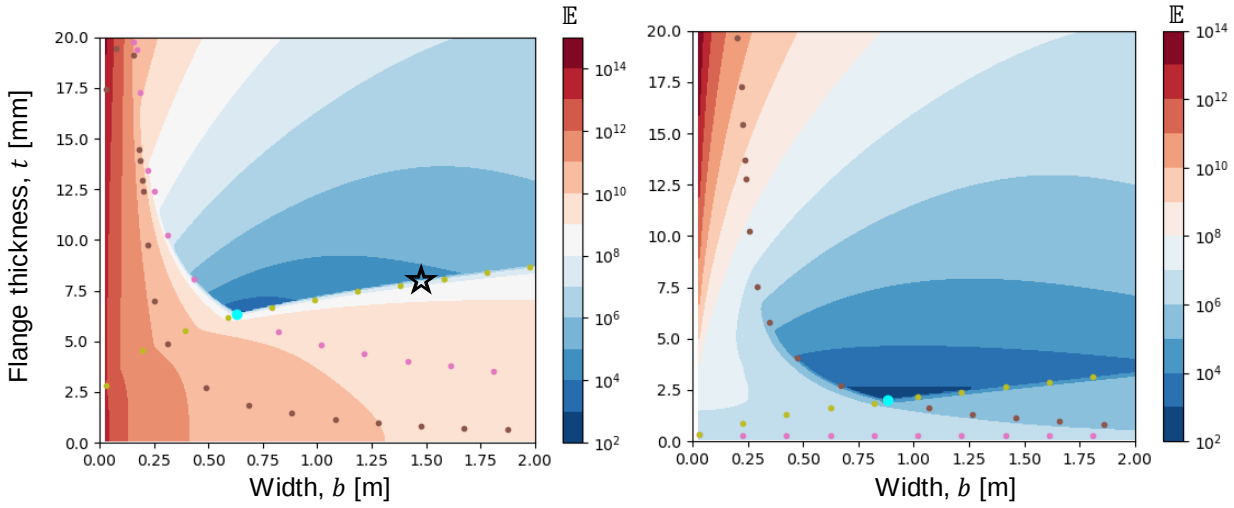

(a) C_S from (16), harmonic ground motion

(b) C_S from (15), UHS $T_r = 475$ years

Figure 26. Contour plots of total residual, $\mathbb{E}$, over a range of t and b for the two different assumed ground motion conditions. The lines show curves of zero residual. The cyan circles show the optimal structure, obtained by minimizing (12). The star shows the TDEA point design.

With the model parameters defined above, the truss mass, natural frequency, and maximum tip displacement are calculated for a range of t and b and visualized as a contour plot in Figure 27. The results for M_{truss} calculated using (3) and shown in Figure 27a visually illustrate that $M_{truss} \propto t^2$, and that M_{truss} is independent of b. The natural frequency (7) of the tower increases with both t and b, remaining relatively low for the range of values considered, as shown in Figure 27b. When the numerator of (7) is negative, Euler buckling occurs due to gravity and ω_n is imaginary; this region is shown in white in Figure 27b. The maximum tip displacement, δ_{tip}, is estimated by $u_{\max} = C_S/(g_M {\omega_n}^2)$ with C_S calculated using (9). The δ_{tip} are relatively large values, as shown in Figure 27c, where the results are truncated at $\delta_{\text{tip}}/H = 0.1$ since small deformations are assumed. Herein, no constraint is placed on δ_{tip}. However, adding a design constraint for dimensional stability is an obvious extension of this work and would lead to designs with larger b or alternative design concepts such as guy wires (see, e.g., [28]).

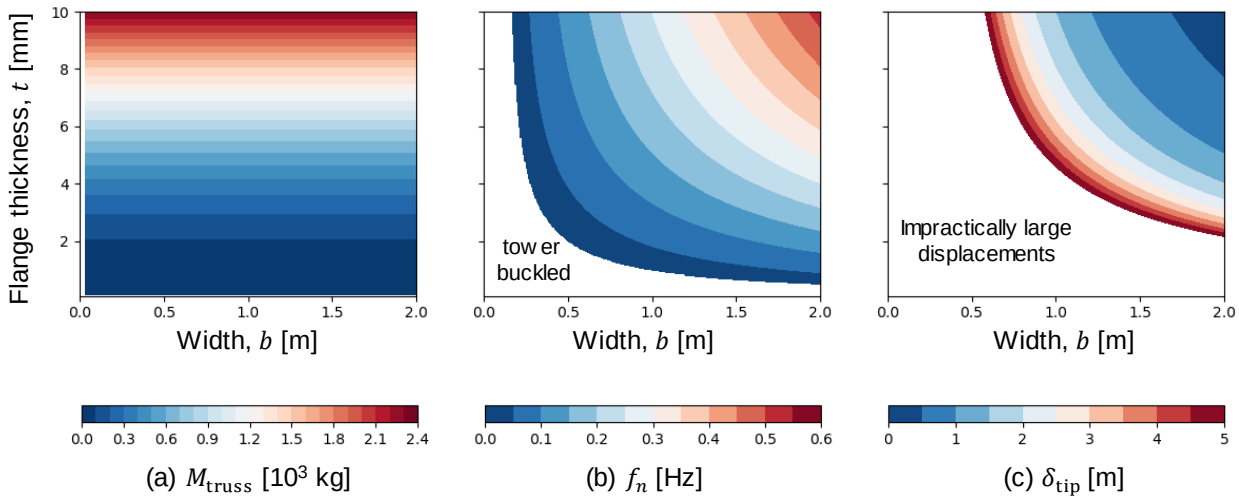

Figure 27. Contour plots of (a) tower structural mass, (b) natural frequency, and (c) maximum tip displacement illustrate trends with the sizing parameters, t and b.

4.5 Assumed Factors: Comparison with TSPD Results

The preliminary sizing routine includes three factors (β_{ah}, β_{ad}, J) that account for the mass of the bracing members and joints since these portions of the structure are not sized directly. Comparing the assumed values for these factors to the inferred values in the TSPD gives some insight into the validity of the assumed values. In the final TSPD, the area reduction factors for the horizontal and diagonal members are $\beta_{ah} = 0.45$ and $\beta_{ad} = 0.25$, which are much lower than the initial assumption of $\beta_{ah} = \beta_{ad} = 0.7$. Therefore, the preliminary analysis is relatively conservative in terms of the mass contribution of the bracing members. For the joint mass penalty, since the JSP and longerons use the same material and have similar cross-sectional dimensions, additional mass at the joints is assumed to be equal to the overlapped length. For the case where $L_w = 2L$, $L = 70$ mm, and $b = 1.5$ m, each node has two joints, so $J = 4L/b + 1 = 1.19$, which is lower than the assumption of $J = 1.3$ used in the preliminary sizing. Future efforts may consider reducing these factors to reduce some of the conservatism. The following parametric studies did not explore the sensitivity to modifying these factors.

5 Parametric Studies

The structural analysis sizing approach described in section 4 is exercised to evaluate some pertinent design trade-offs through a series of parametric studies described in this section. The studies include the effect of material and member cross section.

5.1 Effect of Material

The tower sizing routine is applied using five different materials and three different payloads, M_{PL}, to evaluate the significance of payload mass and material selection on the tower dimensions and mass. The materials include three CFRP composites and two aluminums, with material properties listed in Table 4. The TC1225 material is a T700/LM-PAEK thermoplastic CFRP material used in the TDEA project. The layup is a zero-biased “hard” layup. A second variant of TC1225 is included with a QI layup. The third CFRP material, HM63/8552, has high-stiffness fibers with a zero-biased “hard” layup and an epoxy resin. The resin properties are not required for this sizing, so the results for HM63/8552 are likely representative of what might be achieved with high-stiffness fibers and a thermoplastic resin. To the authors’ knowledge, there is no commercially available high-stiffness fiber thermoplastic composite material system, and no material property data are available for such a material. The aluminum 7075-T6 represents an aerospace-grade aluminum while AL 1100

is meant to represent aluminum produced in-situ on the lunar surface. The tower size parameters are the tower width, b, and longeron cross section thickness, t, with symmetric L-shaped cross sections with $L/t = 10$ held constant. A harmonic acceleration with $\ddot{u}_g/g_M = 0.15$ is used. For the composite materials and AL 1100, $FS = 1.5$, and for AL 7075-T6, $FS = 1.4$ is applied.

Table 4. Material properties for sizing study.

Material	E [GPa]	Strength [MPa]	ρ [kg/m^3]	Reference
HM63/8552	162.0[α]	300[β]	1600	[31]
TC1225, Hard	92.9[α]	393[γ]	1600	[17]
TC1225, QI	45.0[α]	324[γ]	1600	[17]
AL 7075-T6	71.7	538[δ]	2700	[32]
AL 1100	68.9	24[ε]	2700	[32]

[α] Calculated using classical lamination theory from reported mean values
[β] Estimated
[γ] Mean value
[δ] Ultimate
[ε] Yield

The results are summarized in Figure 28 for four tower heights. In each plot, from left to right, each bar corresponds to a different tower configuration (material and payload mass). The plots show the results of the sizing for member thickness t, tower width b, and truss mass M_{truss}. Overall, the trends show t and M_{truss} increasing with payload and more flexible materials. Note that tower width b increases with stiffer materials since cubic truss bays are assumed and stiffer materials reach zero margin in (11) at larger values of b. The tower widths are omitted for AL 1100 since the values are much higher than for the other materials (e.g., $b = 4.5$ m for $H = 50$ m and $M_{PL} = 1000$ kg). For the same reason, all the results for AL 1100 are omitted for $H = 100$ m. For $H = 50$ m, using TC1225 Hard in place of AL 7075-T6 yields a 41% reduction in M_{truss}. The high-stiffness fiber material, HM63/8552, provides an additional 9% mass reduction. M_{truss} increases by about 10 times for towers made with AL 1100 suggesting alternative truss architectures may be appropriate for this class of materials.

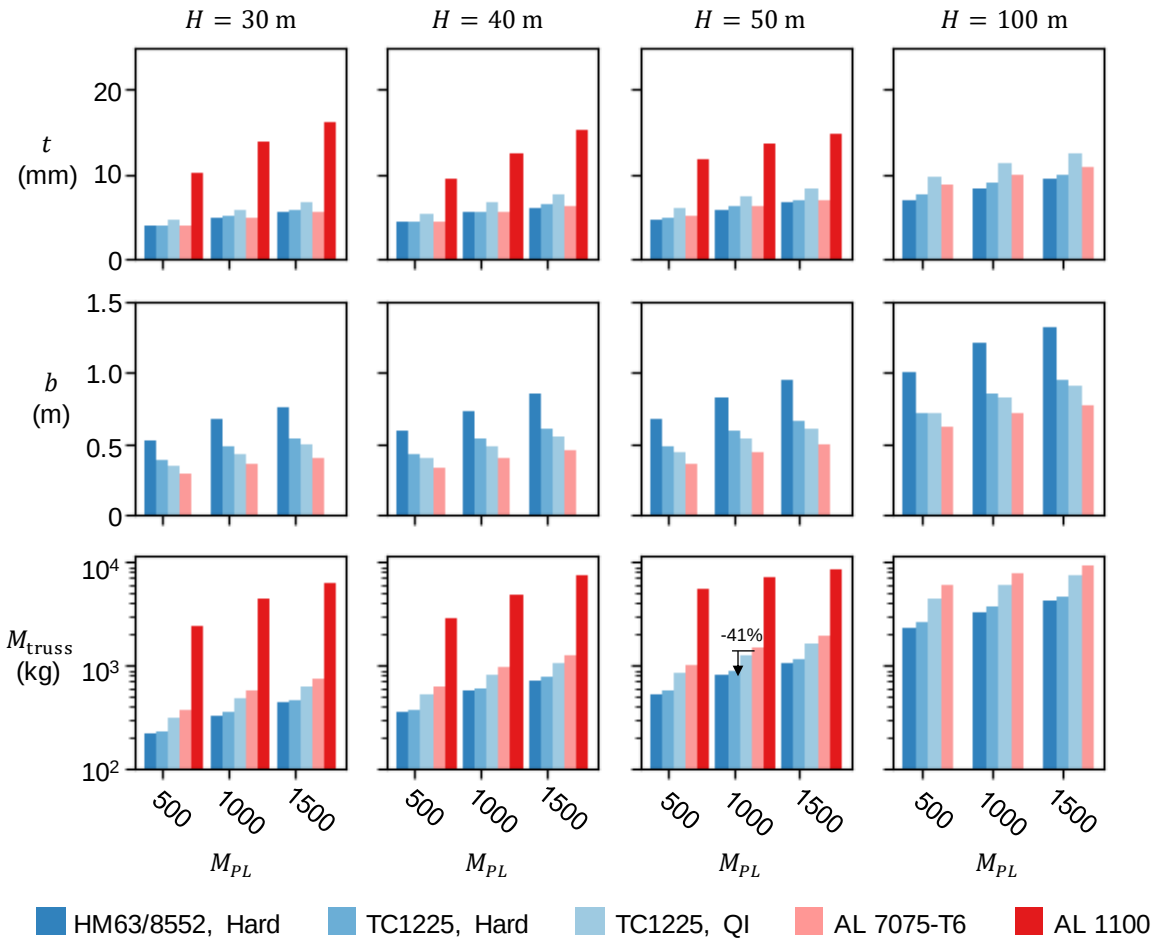

Figure 28. Sizing results for 'L' section designs for different materials, heights, and payload masses.

5.2 Effect of Member Cross Section

The results from a parametric sizing study for four different cross-section shapes are summarized in Figures 29 and 30 for the two assumed moonquake load conditions, harmonic base excitation and UHS with $T_r = 475$ years. Results for 'L' sections are obtained assuming the flange length to thickness ratio is $L/t = 10$. For square tubes, the section width to thickness $w/t = 20$ is assumed, while for round tubes, diameter to thickness $d/t = 50$ is assumed. The CTM cross-section parameters were defined in section 4.2. The results are presented in a similar format to the results for the effect of material properties, with sizing calculated for all combinations of four tower heights H and three payload masses M_{PL}. In all cases, the trends follow the same pattern where the most structurally efficient cross section (CTM) is sized lightest. These results suggest that the TSPD M_{truss} could be reduced by 73% by replacing the 'L' section design with a design using CTMs. Future work should consider the manufacturability and, in the case of the CTM, folding and deployment, of relevant cross-sections.

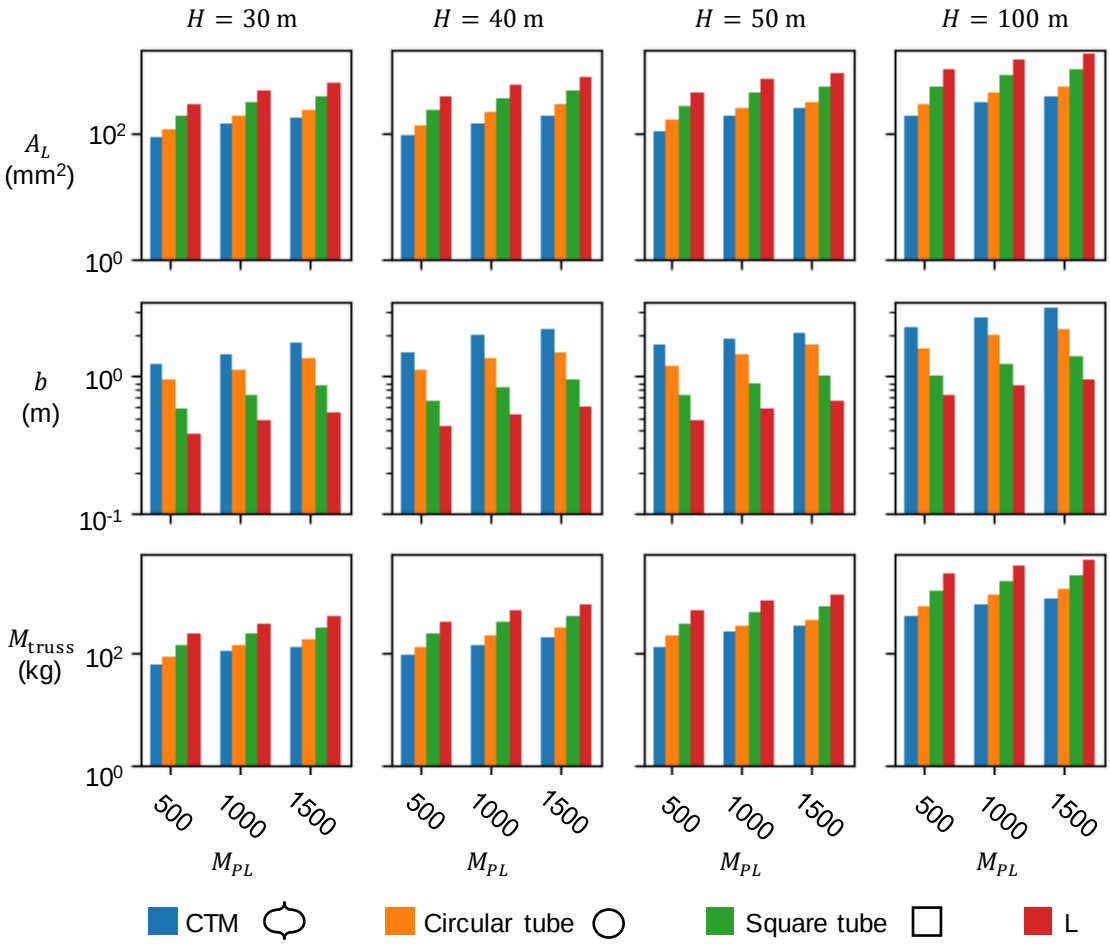

Figure 29. Sizing results for different member cross sections designs for TC1225 Hard material and $\ddot{u}_g/g_M = 0.15$.

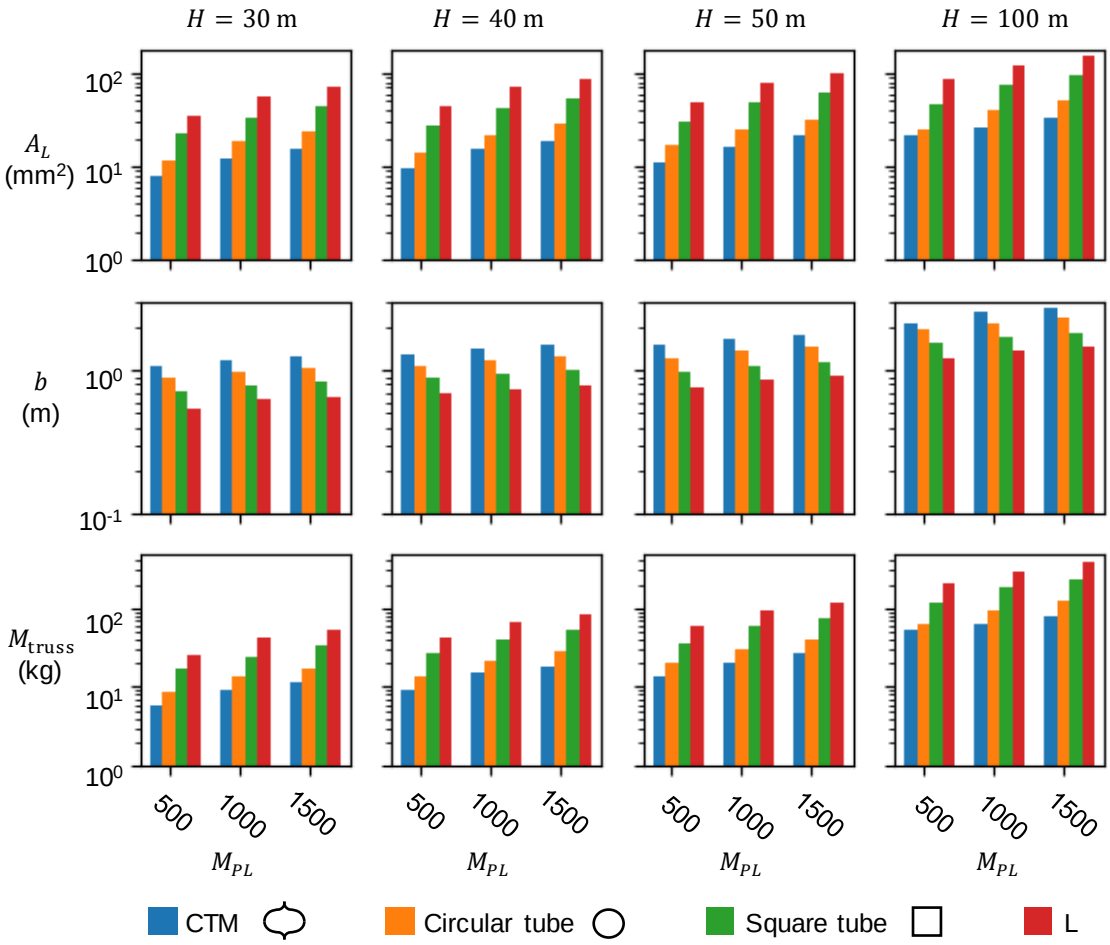

Figure 30. Sizing results for different member cross sections designs for TC1225 Hard material and UHS with $T_r = 475$ yr.

6 Summary

Lightweight tower structures that elevate solar arrays can enable near continuous surface power at the lunar south pole in support of NASA's Moon to Mars Objectives. As part of NASA's Thermoplastics Development for Exploration Applications (TDEA) project, a tower structure point design was developed, focusing on structural integrity of an all-thermoplastic CFRP design that can be assembled robotically by welding the members together at the truss nodes. This report described the tower structural analysis and sizing conducted by the TDEA team.

The tower structure design requirements established in TDEA were summarized. The design requirements are categorized into priority requirements addressed in the TDEA project (A.#) and additional requirements likely necessary for successful flight, but out of scope for TDEA (B.#). Six priority 'A' requirements and sixteen out-of-scope 'B' requirements were identified and discussed.

An approach was developed and applied for structural sizing of truss towers subjected to base excitation from moonquakes. Preliminary sizing was conducted by extending previously developed sizing expressions based on beam theory [5, 6, 16]. The structural sizing routine accounts for Euler buckling of the tower and longerons and strength of the longerons. Detailed design and analysis iterations followed to develop the point design, referred to as the thermoplastic space point design (TSPD). The detailed analysis revealed the importance of manufacturing-driven design details (corner fillet) and joint stiffness in achieving positive margins.

The TSPD was shown structurally feasible based on the analysis results. An evaluation was provided to assess the TSPD based on available test data.

The preliminary sizing routine was further developed for an alternative definition of moonquake loads and additional structural cross section shapes. Verification was performed through comparison with finite element analysis results and shows good agreement. A parametric study was conducted to assess the sensitivity of the design to material properties and cross section shape. The results show that high-stiffness materials such as CFRP save significant mass compared with AL 7075-T6. Considering assumed properties for in-situ sourced aluminum, towers constructed from such material will likely require an order of magnitude more massive structure and perhaps a different truss architecture. Closed cross section shape for the truss members result in significantly lighter truss structures, however, they conventionally have poor volumetric packaging. Deployable concepts such as the collapsible tubular mast look most promising in this response: they offer extremely high structural efficiency with low packaged volume.

7 References

[1] NASA, "Moon to Mars Objectives," September, 2022.

[2] R. Pappa, C. Taylor, J. Warren, M. Chamberlain, S. Cook, S. Belbin, R. Lepsch, D. Tiffin, B. Doggett, M. Mikulas, I. Wong, D. Long, D. Steinkoening, A. Pensado, J. Blandino and J. Haste, "Relocatable 10 kW Solar Array for Lunar South Pole Missions," NASA/TM-20210011743, 2021.

[3] C. Taylor and R. Pappa, "Vertical Solar Array Technology Project," in *GCD Annual Review*, San Antonio, TX, 2023.

[4] J. G. Daye, A. J. Lee and J. M. Fernandez, "Structural Architectures for Self-Erecting Lunar Towers," in *AIAA SCITECH 2023 Forum, American Institute of Aeronautics and Astronautics*, 2023.

[5] W. R. Doggett, J. Heppler, M. K. Mahlin, R. Pappa, J. Teter, K. Song, B. White, I. Wong and M. Mikulas, "Towers: Critical Initial Infrastructure for the Moon," in *AIAA SciTech Forum*, National Harbor, MD, 2023.

[6] K. Song, M. Mikulas, M. K. Mahlin and J. T. Cassady, "Sizing and Design Tool for Tall Lunar Tower," in *AIAA SciTech Forum*, National Harbor, MD, 2023.

[7] A. C. Bergan, B. Farrokh, A. Satyanarayana, W. Grier, K. N. Segal, J. Chiu and S. G. Miller, "Structural Sizing of a 50-m-Tall Thermoplastic Composite Solar Array Truss Tower Structure for the Lunar South Pole," in *American Society for Composites 39th Annual Technical Conference*, San Diego, CA, 2024.

[8] NASA Technical Standard, "Structural design and test factors of safety for spaceflight hardware, NASA-STD-5001B w/ change 3," 2022.

[9] T. R. Watters, N. C. Schmerr, R. C. Weber, C. L. Johnson, E. J. Speyerer, M. S. Robinson and M. E. Banks, "Tectonics and Seismicity of the Lunar South Polar Region," *The Planetary Science Journal,* vol. 5, no. 1, p. 22, 2024.

[10] T. R. Watters, R. C. Weber, G. C. Collins, I. J. Howley, N. C. Schmerr and C. L. Johnson, "Shallow seismic activity and young thrust faults on the Moon," *Nature Geoscience,* vol. 12, no. 6, pp. 411-417, 2019.

[11] C. Nunn, R. Garcia, Y. Nakamura, A. Mausiak, T. Kawamura, D. Sun, L. Margerin, R. Weber, M. Drilleau, M. Wieczorek, A. Khan, A. Rivoldini, P. Lognonné and P. Zhu, "Lunar Seismology: A Data and Instrumentation Review," *Space Science Reviews,* vol. 216, no. 5, p. 89, 2020.

[12] Y. Nakamura, G. V. Latham and H. J. Dorman, "Apollo Lunar Seismic Experiment—Final summary," *Journal of Geophysical Research: Solid Earth,* vol. 87, no. S01, p. A117–A123, 1982.

[13] S. Ruiz, A. Cruz, D. Gomez, S. J. Dyke and J. Ramirez, "Preliminary approach to assess the seismic hazard on a lunar site," *Icarus,* vol. 383, p. 115056, 2022.

[14] W. Grier, A. Stark, R. Wiggins and R. Amundsen, "Thermoplastic Space Point Design (TSPD) Tall Tower Lunar Thermal Analysis," in *Annual Thermal and Fluids Analysis Workshop (TFAWS)*, Cleveland, OH, August 26, 2024.

[15] L. Taylor, H. Schmitt, W. Carrier and M. Nakagawa, "Lunar Dust Problem: From Liability to Asset," in *1st Space Exploration Conference: Continuing the Voyage of Discovery, in Space Exploration Conferences*, Orlando, Florida, 2005.

[16] K. Song, A. Stark, R. Amundsen, M. Mikulas, M. K. Mahlin and J. T. Cassady, "Sizing, Buckling, and Thermal-Structural Analysis of Tall Lunar Tower," in *ASCEND 2023*, Las Vegas, NV, 2023.

[17] R. Mohanty, S. P. Kumar, S. T. G. Raghukanth and K. J. P. Lakshmi, "The Long-Lived and Recent Seismicity at the Lunar Orientale Basin: Evidence From Morphology and Formation Ages of Boulder Avalanches, Tectonics, and Seismic Ground Motion," *Journal of Geophysical Research: Planets,* vol. 125, no. 12, pp. 1-29, 2020.

[18] S. S. Rao, Mechanical Vibrations, Pearson Prentice Hall, 2003.

[19] P. H. Wirsching, T. L. Paez and K. Ortiz, Random Vibrations: Theory and Practice, Courier Corporation, 2006.

[20] A. de M. Wahrhaftig, R. M. L. R. F. Brasil and J. M. Balthazar, "The first frequency of cantilevered bars with geometric effect: a mathematical and experimental evaluation," *Journal of the Brazilian Society of Mechanical Sciences and Engineering,* vol. 35, no. 4, pp. 457-467, 2013.

[21] E. Lian, "Medium Toughness PAEK thermoplastics Toray (Formerly TenCate) Cetex TC1225 (LM PAEK) T700GC 12K T1E Unidirectional Tape 145 gsm 34% RC Qualification Material Property Data Report, CAM-RP-2019-036 Rev A," NIAR, Wichita, KS, 2021.

[22] Siemens AG, *Femap: Version 2023.*

[23] Siemens AG, *Simcenter Nastran: Version 2212.*

[24] Dassault Systèmes Simulia Corporation, *Abaqus Online Documentation: Version 2019,* 2019.

[25] Toray Advanced Composites, "Toray Cetex TC1225 Product Data Sheet," [Online]. [Accessed 11 6 2024].

[26] A. Turon, C. G. Dávila, P. P. Camanho and J. Costa, "An engineering solution for mesh size effects in the simulation of delamination using cohesive zone models," *Engineering Fracture Mechanics,* vol. 74, no. 10, 2007.

[27] ASTM Standard D5868-01, "ASTM Standard D5868-01. Standard Test Method for Lap Shear Adhesion for Fiber Reinforced Plastic (FRP) Bonding," in *Annual Book of ASTM Standards*, ASTM Int., 2014.

[28] B. Tijs, M. Doldersum, A. Turon, J. Waleson and C. Bisagni, "Experimental and numerical evaluation of conduction welded thermoplastic composite joints," *Composite Structures,* p. 114964, 2022.

[29] C. Patiño, S. Ruiz, D. Gomez, A. Cruz, S. J. Dyke and J. Ramirez, "Seismic assessment of a long-term lunar habitat," *Acta Astronautica,* vol. 214, pp. 414-426, 2024.

[30] NASA JPL, "The Farside Seismic Suite," [Online]. Available: https://www.jpl.nasa.gov/missions/the-farside-seismic-suite. [Accessed 14 6 2024].

[31] J. M. Fernandez and C. E. Volle, "Corrugated Rollable Tubular Booms," in *SciTech 2021*, Virtual, 2021.

[32] Y. Xiang and X. G. Gong, "Efficiency of Generalized Simulated Annealing," *Physical Review,* vol. 62, p. 4473, 2000.

[33] SciPy documentation, v1.13.0, "scipy.optimize.dual_annealing," [Online]. Available: https://docs.scipy.org/doc/scipy/reference/generated/scipy.optimize.dual_annealing.html. [Accessed 3 May 2024].

[34] Hexcel, "HexTow HM63 Carbon Fiber," 2023. [Online]. Available: https://www.hexcel.com/user_area/content_media/raw/HM63_Aerospace_HexTow_Data Sheet.pdf. [Accessed 20 5 2024].

[35] The Engineering ToolBox (2008), "Aluminum Alloys - Mechanical Properties," [Online]. Available: https://www.engineeringtoolbox.com/properties-aluminum-pipe-d_1340.html. [Accessed 20 5 2024].

[36] K. Segal, B. Farrokh, D. Sleight, R. Matarese, D. Paddock, R. Allen, H. Gokce and H. Bryn, "3D woven composite end ring for SLS class structures; design development, manufacturing, and verifications," in *The Composites and Advanced Materials Expo*, Anaheim, CA, September 23-26, 2019.

[37] Mathworks, "Color-Based Segmentation Using the L*a*b* Color Space," 2021. [Online]. Available: https://www.mathworks.com/help/images/color-based-segmentation-using-the-l-a-b-color-space.html.

[38] "ASTM Standard D5379. Standard Test Method for Shear properties of Composite Materials by the V-Notched Beam Method," in *Annual Book of ASTM Standards*, ASTM Int., 2012.

[39] "ASTM Standard D7078. Standard Test Method for Shear Properties of Composite Materials by V-Notched Rail Shear Method," in *Annual Book of ASTM Standards*, ASTM Int., 2020.

[40] P. N. Poulsen, J. F. Olesen and M. Baandrup, "Truss optimization applying finite element limit analysis including global and local stability," *Structural and Multidisciplinary Optimization,* vol. 62, no. 1, pp. 41-54, 2020.

8 Appendix A: Investigation of Cable Stayed Designs

As indicated in section 3.1.4, some cable-stayed tower designs were considered but were not ultimately pursued for the TSPD. The implementation of cables, cable pre-tensioning, etc. on the lunar surface would add more complications which, at the time, were outside the scope of the TDEA project. This section briefly shows that a cable-stayed design is feasible in that it can meet the driving design requirements. As shown in Figure 3, stayed cables are advantageous to reduce the effective height of the tower, hence increasing the fundamental frequency of the tower and ultimately lowering the tip deflection while implementing a narrower footprint and thinner truss members (i.e., a lower mass tower).

In this section two cases are evaluated. In both cases ~50 m towers are represented by massless 1-D beam elements, with effective I_{truss} = 0.02 m^4, and support 1000 kg concentrated mass elements at the tip, as shown in Figure A1. Case 1 is the baseline without cable supports. Case 2 further includes (massless) stayed cables, represented by rod elements (A = 0.002 m^2 and J = 6.5x10^{-7} m^4), as also shown in Figure A1.

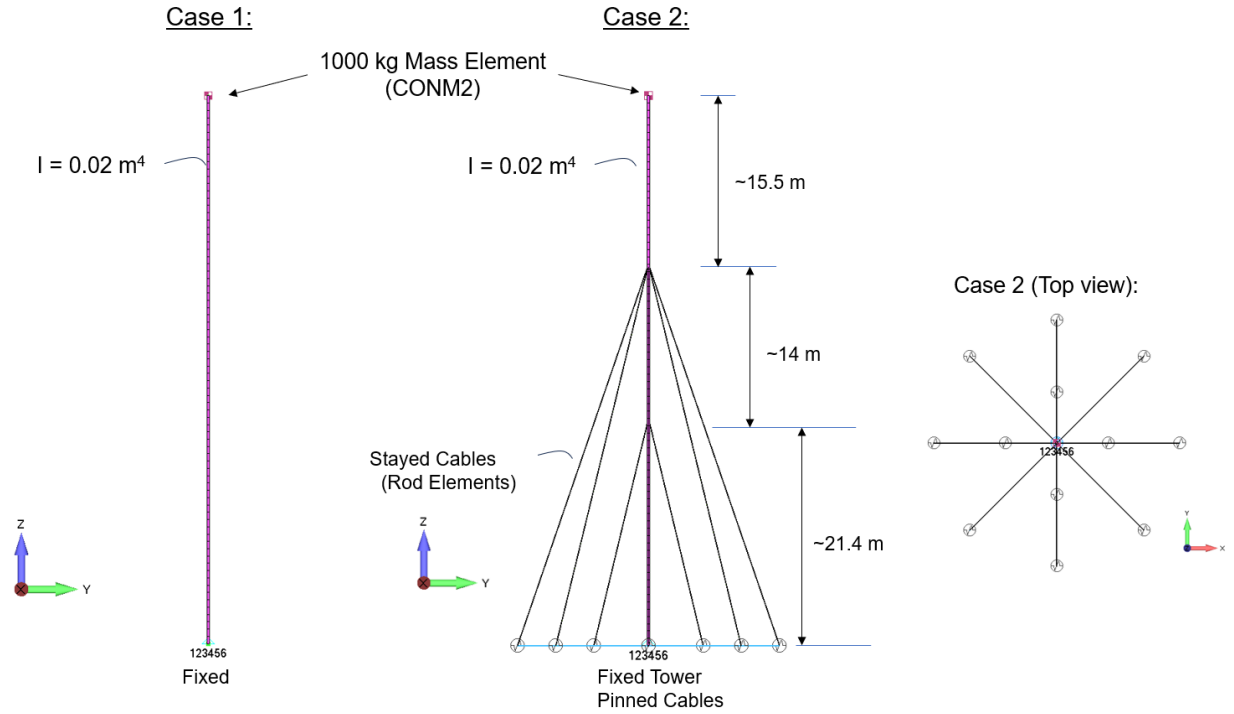

Figure A1. Case 1 (no cables) and Case 2 (with stayed cables) beam tower configurations.

Both cases were subjected to base drive sine vibration input excitation of $\ddot{u}_g/g_M = 1$ from 0.1 Hz to 10 Hz with an assumed Quality (Q) factor of 15 for damping. Figure A2 shows the tip displacement response for both Case 1 and 2.

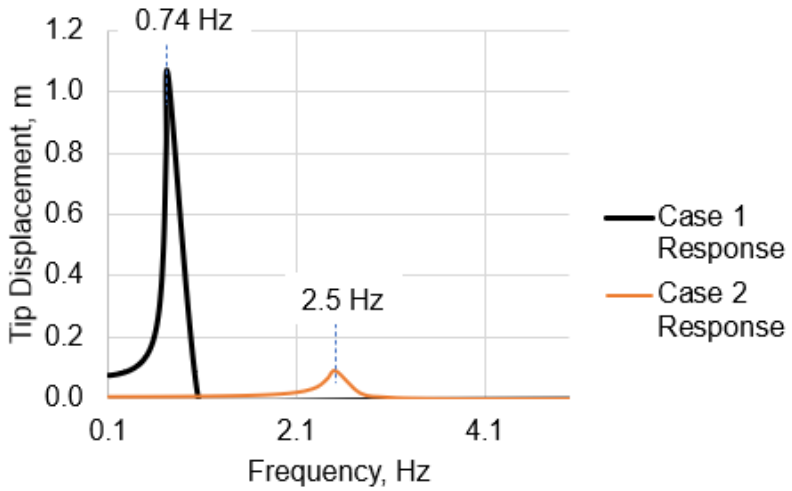

Figure A2. Case 1 and 2 responses to the same level base sinusoidal vibration input.

These results show that the cable-stayed configuration is effective in increasing the fundamental frequency of the tower and reduces the tip displacement to some manageable magnitudes to meet the strength and buckling requirements. This, in turn, results in a smaller tower width b and potentially an overall lighter structure. The mass associated with stayed cables needs to be accounted for in future work to characterize the performance tradeoff. More investigations and detailed analyses are needed to further assess the buckling and strength performance of these cable-stayed design concepts under relevant temperature gradients. Challenges relevant to in-space assembly and cables tensioning mechanisms also need to be addressed and understood.